The Astrophysical Journal, 893:84 (18pp), 2020 April 10 https://doi.org/10.3847/1538-4357/ab7eaa

Absorption-line Abundances in the SMC-like Galaxy UGC 5282: Evidence of ISM Dilution from Inflows on Kiloparsec Scales*

David V. Bowen[1], Todd M. Tripp[2], Edward B. Jenkins[1], Max Pettini[3], Doron Chelouche[4], Renyue Cen[1], and Donald G. York[5]
[1] Princeton University Observatory, Ivy Lane, Princeton, NJ 08544, USA
[2] Dept. of Astronomy, University of Massachusetts, 710 North Pleasant Street, Amherst, MA 01003, USA
[3] Institute of Astronomy, University of Cambridge, Madingley Road, Cambridge, CB3 0EZ, UK
[4] Dept. of Physics, University of Haifa, Mount Carmel, Haifa 31905, Israel
[5] Dept. of Astronomy and Astrophysics, University of Chicago, Enrico Fermi Institute, 5640 South Ellis Avenue, Chicago, IL 60637, USA
Received 2019 September 21; revised 2020 February 13; accepted 2020 March 9; published 2020 April 17

Abstract

We present a Hubble Space Telescope Cosmic Origins Spectrograph spectrum of the QSO SDSS J095109.12 +330745.8 ($z_{em} = 0.645$) whose sightline passes through the SMC-like dwarf galaxy UGC 5282 ($M_B = -16.0$, $cz = 1577$ km s^{-1}), 1.2 kpc in projection from the central H II region of the galaxy. Damped Lyα (DLA) absorption is detected at the redshift of UGC 5282 with log $[N(\mathrm{H\,I})\ \mathrm{cm}^{-2}] = 20.89^{+0.12}_{-0.21}$. Analysis of the accompanying S II, P II, and O I metal lines yields a neutral gas metallicity, $Z_{\mathrm{H\,I}}$, of $[\mathrm{S/H}] \simeq [\mathrm{P/H}] = -0.80 \pm 0.24$. The metallicity of ionized gas from the central H II region $Z_{\mathrm{H\,II}}$ measured from its emission lines is $[\mathrm{O/H}] = -0.37 \pm 0.10$, a difference of $+0.43 \pm 0.26$ from $Z_{\mathrm{H\,I}}$. This difference δ is consistent with that seen toward H II regions in other star-forming galaxies and supports the idea that ionized gas near star-forming regions shows systematically higher metallicities than exist in the rest of a galaxy's neutral interstellar medium (ISM). The positive values of δ found in UGC 5282 (and the other star-forming galaxies) is likely due to infalling low-metallicity gas from the intergalactic medium that mixes with the galaxy's ISM on kiloparsec scales. This model is also consistent with broad Lyα emission detected at the bottom of the DLA absorption, offset by $\sim$125 km s^{-1} from the absorption velocity. Models of galaxy evolution that attempt to replicate population characteristics, such as the mass–metallicity relation, may need to start with a galaxy metallicity represented by $Z_{\mathrm{H\,I}}$ rather than that measured traditionally from $Z_{\mathrm{H\,II}}$.

Unified Astronomy Thesaurus concepts: Quasar absorption line spectroscopy (1317); Interstellar line absorption (843); Dwarf irregular galaxies (417); Metallicity (1031); Damped Lyman-alpha systems (349); Small Magellanic Cloud (1468)

1. Introduction

The history of the universe is essentially the story of how gas, shepherded by the growth of cold dark-matter structures, is turned into stars. The process is cyclic, with star-forming regions inside a galaxy accreting gas from the intergalactic medium (IGM), and the new stars returning energy and metals back into the host's interstellar medium (ISM) and the IGM. This simple ouroboros of inflow and outflow is taken to be a basic ingredient in our attempts to replicate the universe we see today.

Low-mass galaxies provide an important test of our theories about the growth of galaxies and their evolution. Their star-formation history (SFH) appears to be highly dependent on their mass and their (eventual) environment (e.g., Digby et al. 2018; Wright et al. 2019, and references therein), but one way in which they are different from high-mass galaxies is that their shallow potential wells should allow feedback-driven outflows (from stellar and/or supernovae (SNae) winds) to significantly impact their ability to retain metals (e.g., Dekel & Silk 1986; Mac Low & Ferrara 1999; Ferrara & Tolstoy 2000; Garnett 2002; Dalcanton 2007; McQuinn et al. 2018). Star formation can be instigated and, to some extent, sustained from gas flowing into low-mass galaxies without being shocked, along "cold channels" from the IGM (e.g., Kereš et al. 2005; Dekel & Birnboim 2006; Lelli et al. 2014), but some hydrodynamical simulations suggest that much of the gas that is blown out is recycled—clouds gradually cool, return to the galaxy (Christensen et al. 2016), and are then re-heated during the next burst of star formation (Muratov et al. 2017). As a consequence, the expelled metals are not quickly reincorporated back into the next generation of stars, and at $z = 0$, the total gas mass of the inner ISM and the outer circumgalactic medium (CGM) may be similar.

The gas-phase metallicities of the *ionized* gas in star-forming dwarf galaxies can be measured from their H II emission lines, and they certainly have some of the lowest abundances known (e.g., Izotov et al. 2009; Skillman et al. 2013; Hirschauer et al. 2016, and references therein). These abundance estimates can be used to constrain the fraction of metals that have been retained by a host (e.g., McQuinn et al. 2015; Gioannini et al. 2017). The SFH of dwarfs can be probed further by examining the *ratios* of emission-line metallicities: the most well-known example is the change in the nitrogen-to-oxygen ratio (N/O) with oxygen abundance O/H (e.g., Nava et al. 2006; van Zee & Haynes 2006; Berg et al. 2012; James et al. 2017) as nitrogen enrichment transitions from a primary to a secondary contribution, from intermediate-mass stars (e.g., Mollá et al. 2006, and references therein), pollution by Wolf–Rayet stars (Brinchmann et al. 2008), or the mixing of inflowing and

* Based on observations with the NASA/ESA Hubble Space Telescope (HST) obtained at the Space Telescope Science Institute, which is operated by the Association of Universities for Research in Astronomy, Inc., under NASA contract NAS 5-26555.

outflowing gas (Koppen & Hensler 2005; Amorín et al. 2010). A more recent example is the way in which the variation of the carbon-to-oxygen ratio with O/H can be understood as the result of a series of short bursts of star formation (Berg et al. 2019, and references therein).

In this paper, we measure the abundances in *neutral* gas in the nearby galaxy UGC 5282 using absorption lines detected in the spectrum of the background QSO SDSS J095109.12 +330745.8 (hereafter "Q0951+3307," for brevity). A comparison between absorption-line metallicities in neutral gas, $Z_{\rm H\,I}$, measured toward background sources, and those measured from emission lines in ionized gas, $Z_{\rm H\,II}$, from H II regions within a galaxy, is important for several reasons. For sightlines close to H II regions, the method offers the opportunity to compare $Z_{\rm H\,I}$ and $Z_{\rm H\,II}$ directly, to test for differences in calibration of $Z_{\rm H\,II}$ or whether gas within the H II regions is more metal-rich than the rest of the galaxy (Kunth & Sargent 1986). For QSO sightlines further away from star-forming regions, $Z_{\rm H\,II}$ can provide a measurement of ISM and CGM metallicity in areas that cannot be measured in any other way. Such sightlines can probe gas in the outer regions of a galaxy, where, for example, gas may be relatively pristine and/or be accreting from the IGM. In addition, differences in absorption-line profiles seen toward H II regions and toward outlying QSO sightlines could help constrain the extent of outflowing gas in a dwarf galaxy's CGM.

Measurements of $Z_{\rm H\,I}$ toward the *same* H II region used to measure $Z_{\rm H\,II}$ have been made using both the Far Ultraviolet Spectroscopic Explorer (FUSE) and the Hubble Space Telescope (HST), both of which cover the UV region where suitable absorption lines lie (Thuan et al. 2002; Aloisi et al. 2003; Lecavelier des Etangs et al. 2003; Lebouteiller et al. 2004; Cannon et al. 2005; Thuan et al. 2005; Lebouteiller et al. 2006, 2009, 2013; James et al. 2014; James & Aloisi 2018). To date, however, a comparison that uses $Z_{\rm H\,I}$ measured from a background QSO has only been made once before, toward a probe of the low surface brightness galaxy SBS 1543+593 (Bowen et al. 2005; Schulte-Ladbeck et al. 2005), where $Z_{\rm H\,I}$ and $Z_{\rm H\,II}$ were found to be similar. The difficulty, of course, is finding a QSO bright enough to be observed in the UV with HST, behind a galaxy with a low enough redshift that emission lines from individual H II regions can be recorded. The alignment of J0951+3307 with UGC 5282, only 1.2 kpc from its central H II region, provides another opportunity to compare $Z_{\rm H\,I}$ and $Z_{\rm H\,II}$ in a low-mass galaxy. These observations were made as part of an HST program (GO 12486) designed to search for absorption from several QSO-dwarf galaxy pairs, and this paper presents the first results from that program.

This paper is organized as follows. Section 2 discusses the properties of UGC 5282, including an image of the galaxy (Section 2.2), an estimation of its star-formation rate (SFR; Section 2.3), and a simple discussion of its environment Section 2.4. The metallicity of the central H II region measured from its emission lines is discussed in Section 3. The HST Cosmic Origins Spectrograph (COS) observations of J0951 +3307 are presented in Section 4, which discusses the damped Lyα (DLA) absorption (Section 4.2) from UGC 5282, the corresponding weak metal-line absorption, the resulting absorption-line abundances (Section 4.3), and several consistency checks of the derived abundances (Section 4.4). The Lyα emission detected in the damped Lyα absorption trough is presented in Section 4.5. The paper concludes in Section 5 with a discussion of the difference in $Z_{\rm H\,II}$ and $Z_{\rm H\,I}$ for UGC 5282, and compares the value to those found toward H II regions in other galaxies. We discuss the implications of our results in Section 6.

Table 1
Parameters for QSO-galaxy Pair

		Note
Properties of UGC 5282		
R.A., decl. (J2000):	09:51:10.03, +33:07:48.5	1
Heliocentric velocity $v_\odot$:	1577 ± 3 km s^{-1}	2
Adopted Distance D:	22.0 ± 0.2 Mpc	3
SDSS mag g, M_g, $g-r$:	15.5, −16.3, 0.42	4
Johnson mag B, M_B, L:	15.7, −16.0, 0.02L_*	5
Radius $R_{25}(r)$:	34″ ≡ 3.7 kpc	6
$\mu_c(r)$:	21.7 mags arcsec^{-2}	6
H I mass [log($M_\odot$)]:	≃8.5	7
Star-formation Rate:	0.05–0.1$M_\odot$ yr^{-1}	8
Stellar mass [log($M_\odot$)]:	8.5 ± 0.2	9
Specific SFR [log(yr^{-1})]:	−9.5 ± 0.2	8
Halo mass log[M_{200}($M_\odot$)]:	≈10.7	10
Properties of background QSO		
R.A., decl.:	09:51:09.12 + 33:07:45.8	11
Redshift:	0.644	11
Impact parameter ρ:	11.7″ ≡ 1.2 kpc	12

Note. (1) The position of both the brightest central H II region and the SDSS fiber used to measure galaxy's redshift; (2) Velocity cz of the central HII region measured in DR12 of the SDSS (http://skyserver.sdss.org/dr12/en/tools/explore/Summary.aspx?id=1237664667895398539); (3) Distance derived from the Tully–Fisher I-band spiral luminosity-rotation correlation listed in the Cosmicflows-3 Distances database (http://edd.ifa.hawaii.edu/) by Tully et al. (2016). This is 10% smaller than would be inferred from the galaxy's velocity relative to the Cosmic Microwave Background assuming a concordance cosmology; (4) SDSS de-reddened petroMag magnitude and color, and an absolute magnitude assuming D; (5) Johnson magnitudes converted from de-reddened SDSS modelMags using the prescription given by Lupton at http://classic.sdss.org/dr7/algorithms/sdssUBVRITransform.html. We assume $M_* = -20.4$ from Norberg et al. (2002); (6) Results from ellipse fitting to r-band APO image; (7) $M_{\rm H\,I} = 2.36 \times 10^5\ D^2$(Mpc) $I_{21}\ M_\odot$, where I_{21} is taken from Aricebo scans available at http://www.cv.nrao.edu/~rfisher/Arecibo/Profiles/U-05282.109700365.html, although no errors are cited. (8) This paper—see Section 2.3; (9) Using M/L ratios for dwarf galaxies given by Herrmann et al. (2016) and assuming no errors in the SDSS mags; (10) From the assumed stellar mass using Figure 1 of Wright et al. (2019); (11) Data from SDSS DR12 (http://skyserver.sdss.org/dr12/en/tools/explore/Summary.aspx?id=1237664667895398537); (12) The distance between the QSO sightline and the central H II region, which we take to be close to the center of the galaxy.

2. UGC 5282 and Its Environment

2.1. Galaxy Properties

A collation of some of the properties of UGC 5282 and J0951+3307 is given in Table 1. For comparison, the stellar mass and the H I gas mass of the Small Magellanic Cloud (SMC) are both log[M($M_\odot$)] ≃ 8.7 (McConnachie 2012). Hence, UGC 5282 is quite similar to the SMC. The association of the QSO and the galaxy was found through a cross-correlation of QSOs discovered by the Sloan Digital Sky Survey (SDSS) as part of Data Release 5 (DR5), with faint galaxies cataloged by SDSS that had no redshifts. We obtained a spectrum of UGC 5282 using the Dual Imaging Spectrograph (DIS) at the 3.5 m Apache Point Observatory

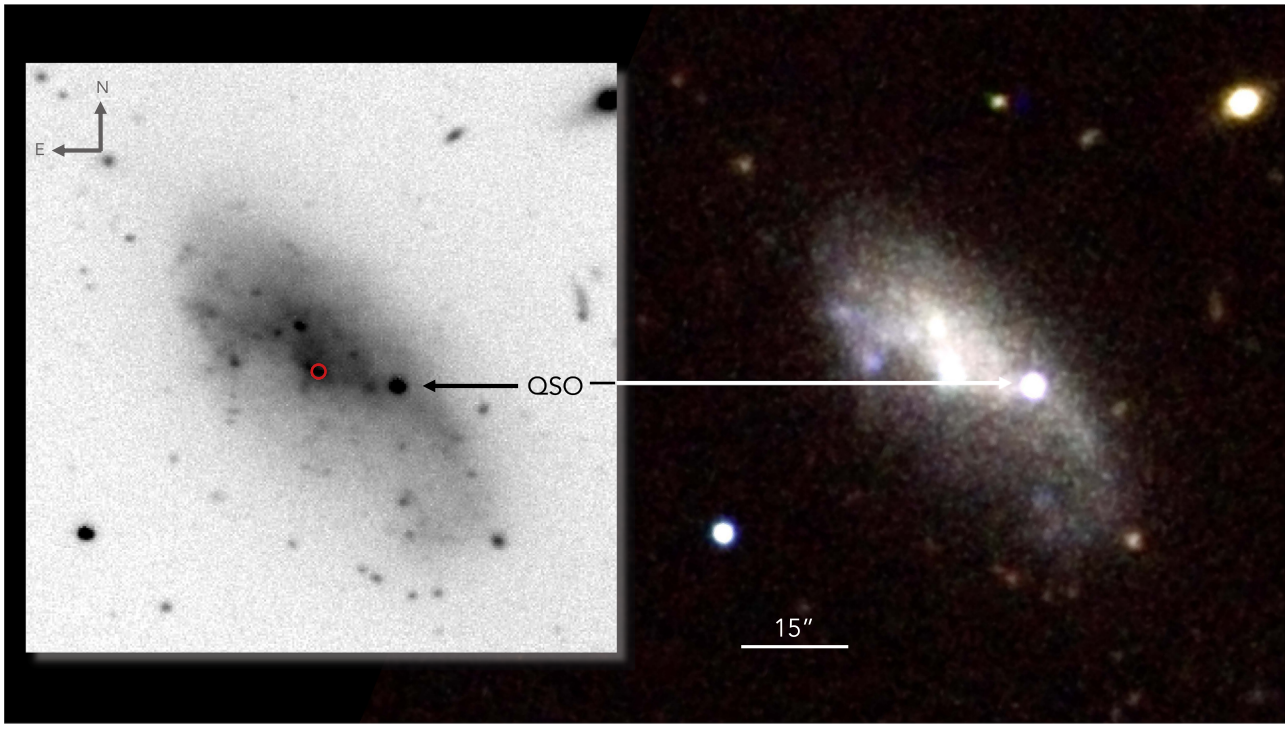

Figure 1. Left, inset: *r*-band image of UGC 5282 taken at APO. Shown in red is a 1″ radius circle corresponding to the size of the SDSS fiber used to measure the redshift of the galaxy, placed at the cataloged position of the fiber. We take this to be the center of the galaxy. Right: False-color image of the galaxy using SDSS *g*-, *r*-, and *i*-band data. These filters were selected because the galaxy is barely detected in the *u*- and *z*-bands. In this color image, the data have been smoothed and scaled specifically to highlight structure in the galaxy. The 15′ scale shown at the bottom of the figure corresponds to 1.6 kpc assuming a distance of 22 Mpc to the galaxy.

(APO) telescope on 2007 March 18, and found a redshift from emission lines of $cz = 1550 \pm 10$ km s^{-1}. Subsequently, a higher signal-to-noise ratio (S/N) spectrum was obtained of the central H II region as part of SDSS DR12, with $cz = 1577 \pm 3$ km s^{-1}. In fact, unbeknownst to us at the start of our redshift identification program, the redshift of the galaxy was first determined from single-dish 21 cm observations by Schneider et al. (1990), who found $cz = 1557 \pm 6$ km s^{-1}.

2.2. Galaxy Imaging

We observed UGC 5282 in the *r*-band with the *Seaver Prototype Imaging camera* (SPIcam) at APO on 2011 March 11 for 1200 s. The data were reduced in the normal way for CCD data frames and co-added to produce the image shown in Figure 1. Conditions were not photometric, and the final zero-point for the photometry was obtained by tying magnitudes of objects recorded in our data with their cataloged SDSS magnitudes.

The *r*-band data from APO is deeper than the *r*-band data recorded by the SDSS, but the latter also covers *g*- and *i*-band fluxes, which are recorded with similar S/N. Images from these three bands were smoothed and aligned to produce the false-color image also shown in Figure 1. The colors are selected to highlight interesting features in the galaxy and are not an accurate color representation.

Both images show that UGC 5282 is morphologically irregular, though there is some indication of a disturbed disk-like structure in the stellar distribution. Simulations of dwarf galaxies show that gas disks start to appear at stellar masses similar to UGC 5282 (e.g., El-Badry et al. 2017), so the existence of a disk for this galaxy is consistent with such models. The bulk of the emission is in the northeast half of the galaxy, which contains several knots of emission from H II regions, two of which are very blue. We use the brightest H II region, observed by SDSS, to define the center of the galaxy. Fainter H II regions exist in the southwest of the galaxy, but the flux from the southeast quadrant is noticeably less than from the rest of the galaxy.

An *r*-band surface brightness profile for UGC 5282 was constructed from the APO image using the `ISOPHOTE` package (Jedrzejewski 1987; Milvang-Jensen & Jørgensen 1999) in version 2.1.6 of PyRAF. The fitted ellipses were constrained to have the same center, i.e., the central H II region. Extrapolating the profile to the center of the galaxy gives the central surface brightness $\mu_c(r)$ listed in Table 1.

2.3. Star-formation Rate of UGC 5282

We estimate the SFR of UGC 5282 based on two different methods. The first utilizes Galaxy Evolution Explorer (GALEX; Martin et al. 2005) images. We retrieved both the FUV and NUV data from the GALEX Archive and measured, with the QSO masked out, magnitudes $m(\mathrm{FUV}) = 17.5 \pm 0.1$ and $m(\mathrm{NUV}) = 17.1 \pm 0.1$ for the entire galaxy. We corrected these magnitudes for Milky Way extinction assuming an extinction $A_{\mathrm{FUV}} = 8.1\ E(B-V)$ mag (Cardelli et al. 1989) and a reddening of $E(B-V) = 0.01$ (Schlegel et al. 1998). Correcting for extinction by dust in UGC 5282 itself, however, is more difficult. The total infrared-to-UV flux is often an indicator of UV extinction as it measures the total stellar emission that has been absorbed and then re-radiated by dust, relative to the UV light observed from stars directly. The only infrared (IR) data that exists for UGC 5282 comes from the

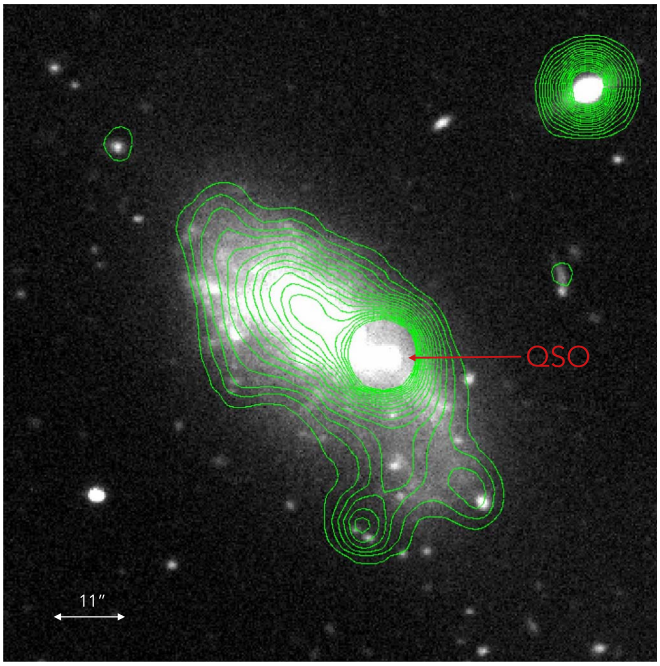

Figure 2. The APO *r*-band image shown in Figure 1 with 3.4 μm contours from WISE data superimposed. The contours are linear and range from 1.0–5.9 μJy.

Wide-Field Infrared Survey Explorer (WISE; Wright et al. 2010). The galaxy is detected in Band-1 (Figure 2) and Band-2 (3.4 & 4.6 μm, respectively), but not at the longer wavelengths (12 & 22 μm); in addition, the QSO is much brighter than the galaxy at 4.6 μm, making a measure of the IR flux from the galaxy unreliable. For these reasons, we decided not to use the WISE data to measure the reddening using the infrared-to-UV flux ratio.

Instead, we first use the reddening toward the central H II region. As we show in Section 3, the spectrum supplied by SDSS can be used to calculate the reddening along the sightline to the star cluster using the ratio of the Balmer lines, which we found gives an extinction $A(\mathrm{H}\alpha) = 0.28 \pm 0.08$ mag. If we assume that this extinction is approximately global, and not confined to the sightline to the H II region, we can convert $A(\mathrm{H}\alpha)$ to A(FUV) by scaling the former by a factor of 5.8, appropriate for the SMC extinction curve (see Section 3). This gives $A(\mathrm{FUV}) \simeq 1.7 \pm 0.5$ mag, leading to a corrected FUV magnitude of 15.8 ± 0.5 mags. The SFR in $M_\odot$ yr^{-1} is then given by Calzetti (2013):

$$\mathrm{SFR(FUV)} = 9 \times 10^{-29}\, L_\nu(\mathrm{FUV})\ (\mathrm{erg\ s^{-1}\ Hz^{-1}}) \qquad (1)$$

or an SFR of $0.1 \pm 0.04 M_\odot$ yr^{-1}.

Our second estimate of the SFR of UGC 5282 comes from observations made using a 100 Å wide narrowband Hα filter attached to SPIcam at APO. A total exposure time of 40 minutes was spent observing the galaxy immediately after the *r*-band observations discussed above were made. After subtracting the *r*-band data to remove the continuum, the central H II region could be seen, along with several of the brightest H II knots visible in Figure 1 and a more diffuse low surface brightness envelope. As noted above, conditions at APO during the observations were not photometric, so to calibrate the Hα image, we matched the counts in a 1″ radius aperture placed on the central H II region with the Hα flux measured by SDSS with the same sized fiber. After using the same extinction correction $A(\mathrm{H}\alpha)$ discussed above,[6] we measure the total Hα flux within $R_{25}(r)$ to be $(9 \pm 0.1) \times 10^{39}$ erg s^{-1}. The SFR is again given by Calzetti (2013):

$$\mathrm{SFR}(\mathrm{H}\alpha) = 5.5 \times 10^{-42}\, L(\mathrm{H}\alpha)\ (\mathrm{ergs^{-1}}), \qquad (2)$$

which gives an SFR of $0.05 M_\odot$ yr^{-1}. The uncertainties in this value are difficult to quantify given the quality of our data: the background of the *r*-band image was not uniform due to contamination by a nearby star, and its subtraction from the Hα image leads to a nonuniform background in the latter. In addition, the calibrations of the SFR for both Equations (1) and (2) are understood to depend on the adopted initial mass function and the metallicities of the stellar population models. The difference of a factor of two between our two estimates of the SFR could well be due to the difficulties in calibrating our narrowband imaging data. We note, however, that Lee et al. (2009) reported that the use of Hα tended to under-predict the SFR compared to values derived from the FUV flux in low-luminosity dwarf galaxies, irrespective of the amount of dust present. If we use the correction suggested in their Figure 5, we would predict an $\mathrm{SFR}(\mathrm{H}\alpha) = 0.06 \pm 0.03$, which is close to the value we measure.

Contours of the WISE 3.4 μm emission are shown in Figure 2, superposed on the APO *r*-band data. Most of the flux comes from the center of UGC 5282, as expected, but there also appears to be additional IR emission to the south and to the southwest, where the *r*-band flux is relatively weak. (These regions are also discernable at 4.6 μm.) It is possible that these areas have regions of star formation that are hidden by dust, which would imply that the SFRs calculated above are only lower limits. A patchy distribution of dust within the galaxy might also go some way in explaining its irregular morphology.

2.4. Galaxy Environment

The HyperLeda catalog (Makarov et al. 2014) lists 23 galaxies within 1 Mpc and ±300 km s^{-1} of UGC 5282, 13 of which are brighter. The dwarf is clearly part of a galaxy group, labeled by Marino et al. (2012) as the "U268" group within the Leo cloud (Tully 1988). The nearest galaxy to UGC 5282 is UGC 5287 (a separation of $\rho = 72$ kpc from UGC 5282), another blue star-forming dwarf, and a magnitude brighter ($M_B = -17.2$) than UGC 5282. Both are likely associated with the bright spiral galaxies NGC 3021 ($\rho = 162$ kpc, $M_B = -19.6$) and NGC 3003 ($\rho = 225$ kpc, $M_B = -20.5$). All of these galaxies are shown in Figure 3.

In comparison to Local Group galaxies, the configuration of the lower-luminosity galaxies UGC 5282 and UGC 5287 shown in Figure 3 is reminiscent of the LMC and SMC's interactions with our Galaxy; although, the distances between the host (NGC 3003) and its satellites are much larger than those between the Magellanic Clouds and the Milky Way (MW). Given the values of M_B for both NGC 3021 and NGC 3003, UGC 5282 and UGC 5287 probably lie just beyond the formers' virial radii and may only be starting on their passage into the DM halo dominated by NGC 3003. In this sense, UGC 5282 may be a younger version of the SMC, seen before its more complex interactions with the MW and the LMC.

[6] For reference, the values of SFR(FUV) and SFR(Hα) assuming no extinction would be 0.02 and $0.04 M_\odot$ yr^{-1}, respectively.

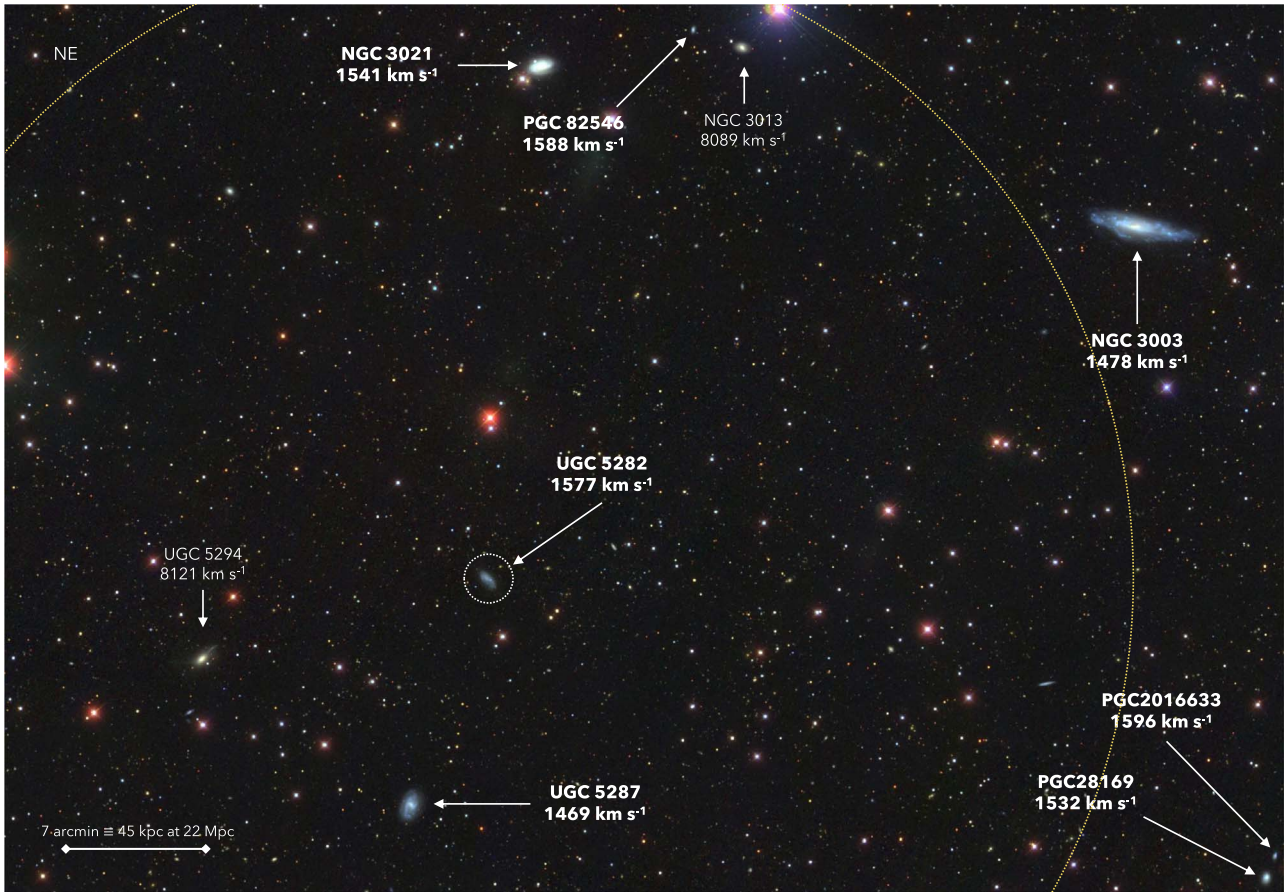

Figure 3. SDSS image of the immediate environment around UGC 5282. The field is dominated by the $M_B = -20.5$ galaxy NGC 3003, which lies 225 kpc from UGC 5282 on the plane of the sky. Its companion is NGC 3021 ($M_B = -19.6$), which lies 198 kpc away. All of the galaxies whose redshifts are known and within ± 400 km s^{-1} of the redshift of NGC 3003 are labeled. The yellow dotted circle represents a radius of 200 kpc centered on UGC 5282 assuming a distance of 22 Mpc from the Milky Way.

For galaxies with masses similar to UGC 5282, $\gtrsim$75% are still forming stars when they lie within 250 kpc of a host galaxy (Geha et al. 2012), so the presence of a star-forming dwarf galaxy close to the more massive galaxies is not unusual. Again, based on comparisons with Local Group dwarf galaxies and results from simulations, UGC 5282, as an irregular dwarf galaxy, has likely been forming stars for most of its history (Gallart et al. 2015) and has only recently begun to be accreted by the two more massive galaxies in the group. Interactions between UGC 5282 and UGC 5287 (Pearson et al. 2018, 2016), as well as stripping (or partial stripping) by the halos of NGC 3021 and 3003 (e.g., Salem et al. 2015; Emerick et al. 2016; Fillingham et al. 2016; Brown et al. 2017, and references therein) might explain the irregular morphology of the galaxy. Alternatively, the on-going star formation in UGC 5282 may actually have been triggered by its interactions with UGC 5287 (Lelli et al. 2014; Stierwalt et al. 2015). We reiterate these ideas in Section 6.

3. Metallicity of the Central H II Region

As noted above, the central H II region was observed by SDSS, with the fiber covering the region shown in Figure 1. The DR12 SDSS spectrum[7] (Plate−MJD−Fiber ID = 5798 −56326−050) shows a continuum rising slowly toward the blue, superimposed with many archetypal H II narrow emission lines. These can be used to determine the H II region's metallicity.

After correcting the spectrum for extinction by the Milky Way, we modeled the continuum using the STARLIGHT[8] spectral synthesis code described by Cid Fernandes et al. (2005). Not surprisingly, given the lack of any significant stellar absorption lines, the fluxes of the emission lines were corrected by only very small amounts. The continuum itself could be modeled with a young ($\sim$(1–3) $\times$ 10^6 yr) population of stars that has a total stellar mass of (1–2) $\times$ 10^6 $M_\odot$. After correcting for the extinction at Hα (see below), the Hα luminosity of the H II region (as covered by the SDSS fiber) is $\log[L(\mathrm{H}\alpha)(\mathrm{erg\ s^{-1}})] = 38.22 \pm 0.01$ and the SFR using Equation (2) is $\log[\mathrm{SFR}(M_\odot \mathrm{yr^{-1}})] = -3.04 \pm 0.01$ for this specific star cluster (and not for the galaxy as a whole).

It is well known that the Balmer emission-line fluxes have fixed ratios with respect to each other under certain assumptions. For Case-B recombination, and assuming electron densities and temperatures typical for an H II region (10^2 cm^{-3} and 10,000 K respectively), ratios of $\mathrm{H}\alpha/\mathrm{H}\beta = 2.85$, $\mathrm{H}\gamma/\mathrm{H}\beta = 0.469$, $\mathrm{H}\delta/\mathrm{H}\beta = 0.260$, etc. are predicted (Hummer & Storey 1987). Deviations from these ratios are taken to be due to dust extinction along a line of sight, with the broadband color excess $E(B-V)$ given by (e.g., Momcheva

[7] http://skyserver.sdss.org/dr12/en/tools/explore/Summary.aspx?id=1237664667895398539

[8] http://www.starlight.ufsc.br/

Table 2
Strong-line Diagnostics of the Central H II Region of UGC 5282

Method ID	Method Line Ratios	Method σ_{SL}[a]	12 + log(O/H)	$Z_{H\,II}$[b]	Calibration References
Ar3O3	[Ar III] λ7135/[O III] λ5007	±0.23	8.43 ± 0.10	−0.33 ± 0.11	1
S3O3	[S III] λ9069/[O III] λ5007	±0.25	8.42 ± 0.03	−0.34 ± 0.06	1
S23	([S II] $\lambda\lambda$6716, 6730 + [S III] $\lambda\lambda$9069,9530)/Hβ	±0.10	8.39 ± 0.03	−0.37 ± 0.06	2
N2	[N II] λ6583/Hα	±0.16	8.26 ± 0.01	−0.50 ± 0.05	3
O3N2	([O III] λ5007 x Hα) / ([N II] λ6583 x Hβ)	±0.18	8.27 ± 0.01	−0.49 ± 0.05	3
KK04	f([O II] λ3727, [O III] λ4959, 5007, Hβ, q)	±0.2	8.36	−0.40	4

Notes.
[a] This is the the approximate 1σ dispersion in the calibration of the emission-line-ratio metallicities.
[b] Metallicity of the central H II region in UGC 5282, log(O/H) −log(O/H)$_\odot$ where 12 + log(O/H)$_\odot$ = 8.76 (Lodders 2003). The errors listed in this column are only combined errors from the flux measurements.
References. 1. Stasinska (2006), 2. Pérez-Montero & Díaz (2005), 3. Marino et al. (2013), 4. Kobulnicky & Kewley (2004).

et al. 2013)

$$E(B-V) = \frac{-2.5}{\kappa(\mathrm{H}\alpha) - \kappa(\mathrm{H}\beta)} \times \log_{10}\left[\frac{(\mathrm{H}\alpha/\mathrm{H}\beta)_{\mathrm{obs}}}{(\mathrm{H}\alpha/\mathrm{H}\beta)_{\mathrm{true}}}\right] \quad (3)$$

where κ(Hα) and κ(Hβ) are the values of a dust attenuation curve at the wavelengths of Hα and Hβ and $(\mathrm{H}\alpha/\mathrm{H}\beta)_{\mathrm{true}} = 2.85$. Additional estimates of $E(B-V)$ can be made if other Balmer lines are present using a similar relationship. The extinction for any other line at a wavelength λ is then simply $A(\lambda) = \kappa(\lambda)\ E(B-V)$. We estimated values of κ using the extinction curve given by Gordon et al. (2003) for the SMC, with $R_V = 2.74$, where $R_V = A(V)/E(B-V)$. The measured ratios Hα, Hγ, and Hδ to Hβ gave similar values for UGC 5282, with Hα/Hβ having the smallest errors:

$$E(B-V) = 0.13 \pm 0.04$$

and from which all of the emission lines detected toward the H II region in UGC 5282 were corrected. The extinction at Hα (used in the previous section) was $A(\mathrm{H}\alpha) = 0.28 \pm 0.08$ mags.

After correcting the spectrum for this extinction, we measured the emission-line fluxes and their errors. Fluxes were measured by fitting single Gaussian profiles (except for [O II] λ3727 where both lines of the doublet are blended to show a clearly asymmetric profile—the flux integrated over the whole line was used instead); errors were generated by using a Monte Carlo approach of fitting multiple synthetic constructions of the initial fitted line, with their errors defined by those supplied by SDSS. An additional term $\sigma_c^2 = \sum(\sigma_i^2)$ was added in quadrature to this error in order to account for uncertainties in the background, which can be significant for weak lines, where σ_i is the error at the ith pixel given by the error array, summed over the number of pixels used to define the background. The spectrum shows Balmer lines down to Hζ and many forbidden collisionally excited metal lines. When compared to values that define the commonly used BPT (Baldwin et al. 1981) relationships, the ratios of log([O III]λ5007/Hβ) = 0.20 ± 0.02 and log ([N II]λ6583/Hα) = −1.05 ± 0.03 place the source well within the area of star-forming H II regions.

There are two well-known methods for determining the metallicities of extragalactic H II regions from their emission lines: first, there is the "direct," or "T_e" method, which measures electron temperatures directly from ratios of weak and strong recombination lines arising from atomic levels with substantially different excitation levels, and second, strong emission-line (SELs) ratios can be used, calibrated by using either photoionization models or by using H II regions for which O/H has already been measured using the T_e method. In addition, it is possible to use recombination lines (RLs) of heavy elements to RL lines of hydrogen to measure O/H (the "RL method"), but the metal lines are often too weak to be observed in many extragalactic objects.

The resolution and S/N of the SDSS spectrum is too low to permit detection of weak auroral lines such as [O III] λ4363 or [N II] λ5755, which are often used to calculate T_e in an H II region. We therefore used SEL ratios to measure $Z_{H\,II}$. We avoided using SEL diagnostics, which rely on the [O II] λ3727 line simply because the correction of fluxes from reddening due to internal dust extinction are the most severe in the blue. Fortuitously, the long wavelength range of the SDSS spectrum covers [Ar III] λ7135 and [S III] $\lambda\lambda$9069, 9530 lines in the red. Since S, Ar, and O are all α elements and are produced by the same types of stars, the Ar3O3 and S3O3 indexes calibrated by Stasinska (2006) provide a measurement of the oxygen abundance O/H that should be largely unaffected by chemical evolution effects. The definitions of both indexes are listed in Table 2. Another index that also uses both [S II] and [S III] lines is S23 (Díaz & Pérez-Montero 2000; Pérez-Montero & Díaz 2005). Table 2 shows that Ar3O3, S3O3, and S23 all give consistent results: 12+log O/H ∼8.4, with an error likely dominated by the errors in the index calibration, between ≃ ±0.1 to ±0.25 dex.

Table 2 also lists the [N II] λ6583 line diagnostics N2 and O3N2 (e.g., Alloin et al. 1979; Storchi-Bergmann et al. 1994; Pettini & Pagel 2004; Marino et al. 2013). N2 in particular is highly sensitive to the O/H abundance, and it is largely unaffected by errors in the reddening correction, because of the similarity in the wavelengths of [N II] λ6583 and Hα. Both of these ratios, however, depend on N/O, which can vary with O/H. A significant fraction of the [N II] λ6584 flux may also come from the diffuse ionized ISM along the line of sight and not from the H II region itself (Stasinska 2006). Hence, the N2 and O3N2 ratios may be less suitable for providing a comparison between $Z_{H\,II}$ and $Z_{H\,I}$.

Finally, we also include an estimate of $Z_{H\,II}$ using SEL ratios calibrated from photoionization models by Kobulnicky & Kewley (2004). This index, which we refer to as KK04 in Table 2, uses a combination of the well-known R_{23} emission-line ratio [([O II] λ3727 + [O III] λ4959, 5007)/Hβ] and the ionization parameter q (the ratio of the flux of ionizing photons

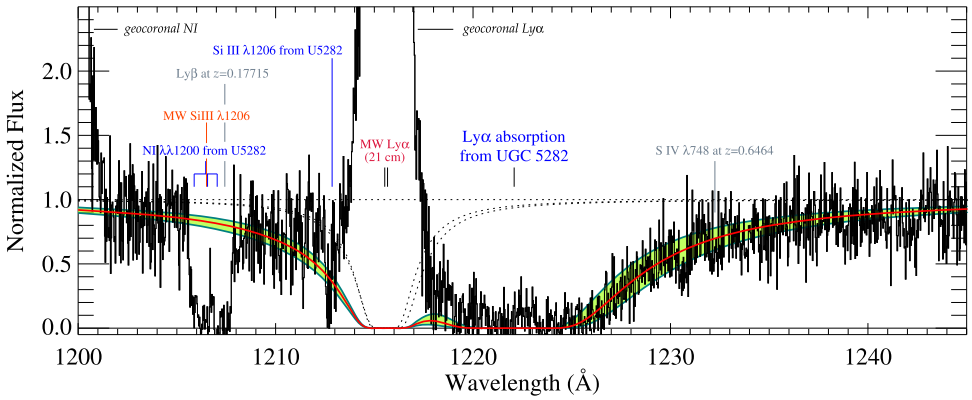

Figure 4. Normalized COS spectrum of the QSO J0951+3307. A composite Lyα absorption-line profile is shown as a red line, which is comprised of absorption from UGC 5282 at $v = 1581$ km s^{-1} with log N(H I) = 20.89 (+0.12, −0.21) and two components inferred from 21 cm emission-line measurements (black dotted lines) at −35 and 0 km s^{-1} with log N(H I) = 19.79 and 19.70, respectively. The region shown in green corresponds to profile fits made to data normalized by continuum fits that are 1σ deviant from the best-fit continuum. The geocoronal emission lines from Lyα and N I are marked, as well as the wavelengths of other detected absorption lines.

to the hydrogen density). Their low-metallicity branch gives unique values of O/H providing log(O/H) $\lesssim$ 8.5, which, from the other SEL ratios given in Table 2, appears to be true for UGC 5282. While we have avoided using the [O II] λ3727 line for the reasons mentioned above, López-Sánchez et al. (2012) have suggested that the KK04 index is unique in being able to match values measured from the RL method. We find the KK04 index for UGC 5282 to be between the Ar3O3 and S3O3 ratios, and the ratios that use the [N II] line, N2 and O3N2.

4. COS Observations and Data Reduction

Observations were made with COS using the 2.″5 diameter Primary Science Aperture (PSA) and the G130M grating at Life Position 1. J0951+3307 was observed for six orbits, broken into two visits, with total exposure times of 8192 s using the grating centered at 1291 Å, and 8192 s when centered at 1327 Å; these two positions were chosen to provide some data in the gap between the two segments of the photon-counting microchannel plate detector after coadding all of the exposures (Green et al. 2012).

Data were processed with version 3.1.7 of the CALCOS pipeline software. The post-processed coaddition of all of the sub-exposures has been discussed in detail in Bowen et al. (2016) and is not repeated here. We initially selected the QSO as a potential HST target given its GALEX FUV flux listed in *General Release* GR4 as 104 ± 8μJy. Subsequent GALEX catalog releases, however, did not contain the QSO, only the foreground galaxy. We measured a flux from the COS data of F_λ(1400 Å) = 3 × 10^{-16} erg cm^{-2} s^{-1} Å^{-1}, only a fifth of that expected (equivalent to F_ν(FUV) = 20 μJy in the GALEX FUV band). Either the QSO FUV flux is variable, or (more likely) the original catalog overestimated the flux due to additional light from the foreground galaxy. The resulting S/N ratio of the spectrum was consequently lower than expected, ∼4 per (rebinned) 0.03 Å pixel.

Comparison between features in the spectra obtained in the two HST visits showed a clear shift of ∼5 rebinned pixels, or 0.15 Å between each. The spectrum from the second visit was shifted to match that of the first, as the latter was found to show absorption lines from low-ionization gas in the Milky Way that best matched the velocity of 21 cm emission features seen in the Leiden/Argentina/Bonn (LAB) Survey of Galactic H I (Kalberla et al. 2005).

Portions of the final co-added COS spectrum are shown in Figures 4–6, including the damped Lyα absorption at the redshift of UGC 5282 (Figure 4), as well as selected metal lines affiliated with the H I absorption (Figures 5–6).

4.1. Line Identification and Profile Fitting

The procedures for fitting the continuum of the spectrum, for measuring the physical parameters of the detected absorption lines—their Doppler parameters b, line-of-sight velocities v, and column densities N—and the methods used for determining errors in these values, are discussed in detail in Bowen et al. (2008, 2016) and are only summarized here.

We normalized the final co-added spectrum by fitting Legendre polynomials (e.g., Sembach & Savage 1992) to areas free of features. Along with the best-fit continuum, we generated ±1σ "upper" and "lower" error "envelopes" to represent the deviations that accompany the best fit. For absorption lines of interest, we constructed theoretical Voigt line profiles from initial estimates of v, N, and b, and allowed these parameters to vary until a minimum in χ^2 between profile and data was reached. Oscillator strengths for the lines were taken from Morton (2003), Kisielius et al. (2014) (S II), Federman et al. (2007) (P II λ1152), or Brown et al. (2018) (P II λ1301). Theoretical line profiles were convolved with COS Line Spread Functions (LSFs) constructed by interpolating LSF tables[9] to the relevant wavelength. Errors to the parameters were calculated using a Monte Carlo approach, in which 400 synthetic spectra were constructed from the best-fit profile using the error arrays and re-fit to give new values of v, N, and b. These errors were combined in quadrature with the differences between the best-fit values found when using the spectrum normalized by the upper and lower continuum fits.

4.2. Damped Lyα Absorption in UGC 5282

Figure 4 shows the Lyα absorption from UGC 5282. The line is clearly damped and blended with strong Lyα from the

[9] Available online at the Space Telescope Science Institute (http://www.stsci.edu/hst/cos/performance/spectral_resolution/).

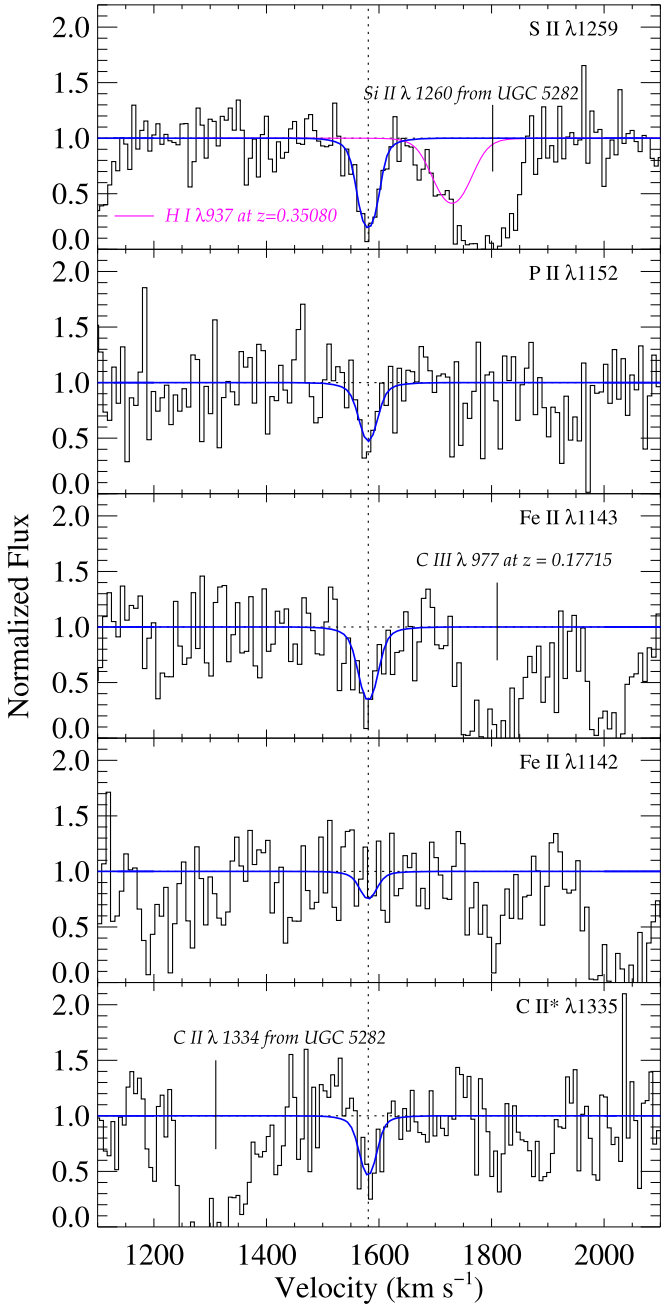

Figure 5. Sections of the normalized COS spectrum of J0951+3307 featuring the set of relatively weak absorption lines from different ions at the velocity of UGC 5282. Other significant intervening lines are also indicated.

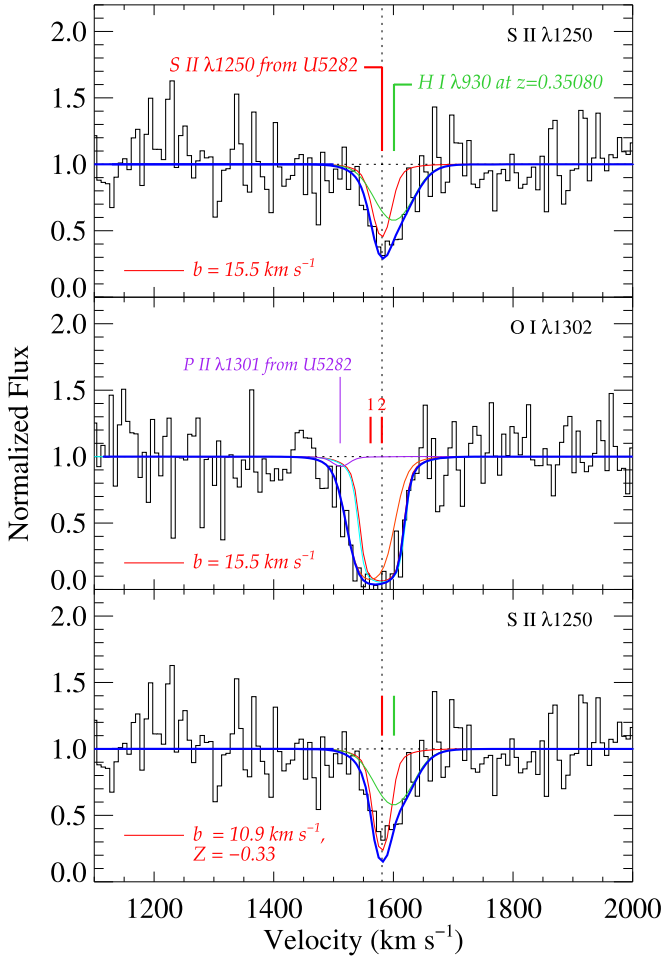

Figure 6. Predicted profiles of S II λ1250 and O I λ1302 lines arising from UGC 5282. *Top panel*: the theoretical line profile for the S II λ1250 line assuming N(S II), v and b derived from the S II λ1259 line, given in Table 3, is shown as a red line. The S II line is blended with a higher-redshift H I Lyman series line (predicted as the green line given the measured H I and b-value from other Lyman lines at the same redshift), which makes the final S II line profile uncertain, but the predicted blend of the S II and H I lines, shown in blue, matches the data well. *Middle panel*: a theoretical line profile fit for the O I line requires two components, assuming that one of the components (labeled "2" in this figure) has the same v and b values given in Table 3. The two components are shown as red lines, and their composite blend in blue. Although the fit appears to match the data well, component 2 is saturated and insensitive to N (O I): the cyan line shows the predicted line profile of component 2 when it has the value of N(O I) expected given the same metallicity $Z_{\rm H\,I}$ derived from the S II λ1259 line, which is 0.3 dex smaller than the best-fit line profile shown in red. The two profiles are largely indistinguishable. Also shown in purple is the predicted profile of the P II λ1301 line based on the values of the P II λ1152 line given in Table 3. *Bottom panel:* the same S II λ1250 line shown in the top panel but showing a profile for an absorbing cloud that has the same metallicity as the central H II region, $Z_{\rm H\,II}$(O) = −0.37, which requires b = 10.9 km s^{-1}. The profile is clearly a poorer match to the data than the best-fit model shown in the upper panel, but the difference is small.

Milky Way (MW). In order to define the velocity of the absorption system from UGC 5282, we first fitted four weak, low-ionization lines that are expected to be associated with high column density H I: S II λ1259, P II λ1152, Fe II λ1143, and C II* λ1335, along with the part of the spectrum where Fe II λ1142 was expected, but not detected. These metal lines were fitted simultaneously, allowing b and v to vary, but requiring that their final values be the same for each ion. This produced an absorption velocity of 1581 km s^{-1} that we used to fit the Lyα absorption from UGC 5282. These lines are discussed in more detail in Section 4.3 below.

Our model for the Lyα absorption shown in Figure 4 consists of N(H I) from the MW as measured from two 21 cm emission lines[10] at −35 and 0 km s^{-1} (shown as black dotted lines in Figure 4), as well as the absorption from UGC 5282. The resulting blend of Lyα lines (the red line in Figure 4, with the uncertainty in the continuum fit shown in green) seems inadequate between ≈1210–1212 Å, in that it appears to over-predict the absorption in the blue wing of the DLA line. This may be because of a contribution from flux in the wings of the

[10] Data taken from the LAB survey (https://www.astro.uni-bonn.de/hisurvey/AllSky_profiles/index.php) (Kalberla et al. 2005).

Table 3
Results from Voigt Profile Fits to Weak Absorption Lines from UGC 5282

Ion (X)	Detected[a] Lines	$v = 1581 \pm 3$ km s^{-1} b (km s^{-1})	log[N(cm^{-2})]	N(X)/N(H I) − $Z_\odot$
H I	**λ1216**	⋯	20.89 (+0.12,−0.21)	⋯
	Lines fitted simultaneously to give single b and v values			
S II	λ1250, **λ1259**	15.5 ± 5.9	15.33 (+0.37, −0.15)	−0.82 (+0.39, −0.26)
P II	**λ1152**	15.5 ± 5.9	13.65 (+0.27, −0.24)	−0.78 (+0.30, −0.32)
Fe II	**λ1143**, λ1144, (**λ1142**)[b]	15.5 ± 5.9	15.02 (+0.33, −0.22)	−1.41 (+0.35, −0.31)
C II*	**λ1335**	15.5 ± 5.9	13.86 (+0.27, −0.25)	⋯
	Lines fitted assuming fixed b and/or v			
O I	**λ1302**	15.5	16.51 (+0.49, −0.72)	−1.14 (+0.51, −0.75)
		29.8 ± 17.7[c]	15.15 (+0.55, −0.32)	⋯
Si II	**λ1190, λ1304**	15.5	14.83 ± 0.36	−1.67 (+0.38, −0.42)
		30.0 ± 6.2[c]	14.60 (+0.19, −0.12)	⋯

Notes.
[a] Lines in bold indicate which lines were fit with Voigt profiles;
[b] Fe II λ1142 not detected, but data used to constrain fit;
[c] Additional component at $v = 1562$ km s^{-1}.

geocoronal Lyα emission line and/or a difference in the true N(H I) along the line of sight from that measured from the 21 cm emission lines, which are obtained from observations that have a 0°.6 beam size. It is possible to obtain a better fit in this wavelength range by reducing N(H I) from the MW, but the column density must be 2 dex smaller, with a value $\sim 10^{18}$ cm^{-2} compared to the 10^{20} cm^{-2} measured at 21 cm. Such a value would be unusually low for the disk of the MW, and so contamination from the geocoronal Lyα emission line seems a more likely explanation for the poor fit at these wavelengths. However, beyond ∼1221 Å, a damped Lyα absorption-line profile from UGC 5282 fits the data well; evaluation of N(H I) from the profile fitting is dominated by data at these wavelengths and is unaffected by whether regions to the blue of the geocoronal Lyα line are masked out or included in the fit, or whether the velocity of the absorption from UGC 5282 is allowed to vary or is fixed at the 1581 km s^{-1} discussed above. Our final measurement of N(H I) is given in Table 3.

4.3. Metal-line Column Densities from Weak Lines and Neutral Gas Metallicity

As discussed above, in order to derive column densities from the ISM of UGC 5282, we fitted theoretical Voigt profiles to a selection of weak, unsaturated, metal lines. These are discussed below.

Of the three lines of the S II triplet expected to be found from UGC 5282, S II λ1253 is lost in the blend of Si II λ1260 and S II λ1259 lines from the Milky Way, while the S II λ1250 line is contaminated by H I λ930 at $z = 0.35080$ (we return to this line in Section 4.4). S II λ1259 is uncontaminated by other absorption lines, and it provides the basis of the derivation of N(S II).

Absorption from UGC 5282 is also seen in a single line of P II λ1152, weak C II* λ1335, and in several Fe II lines. Of the three lines of the Fe II λλ1143 triplet, the λ1143.2 line is detected, and the λ1142.4 line is absent. The strongest of the three, λ1144.9 is too strong given the strength of the other two lines and is likely contaminated by another feature that we cannot identify. It is therefore not included in our fitting procedure.

The four lines (and one non-detection) used to derive the column densities are shown in Figure 5. Fitting the lines resulted in a Doppler parameter of $b = 15.5 \pm 5.9$ km s^{-1}; the profiles are shown in blue in Figure 5. All of the parameters derived from the fit are listed in Table 3.

Sulphur is often taken as a proxy for oxygen when deriving gas-phase metallicities, because the O I λ1302 line, which lies nearby in the far-UV, is saturated for high values of N(H I), while weaker O I lines are at (shorter) wavelengths that are not always available. Both O and S are α-elements formed as part of the α-capture process in massive stars ($>10 M_\odot$) and released in SNae IIa, so they are expected to track each other closely. Matteucci & Chiappini (2005) have pointed out that some S may also be produced in SNae Ia, but for Fe/H abundances of <-0.5, the difference in the O/S ratio from solar is <0.08 dex, which, as we shall see, is much less than the errors we derive in this paper. The other problem in assuming that O and S abundances are the same is that the relative O/S ratio may depend on the amount of depletion present. Oxygen is only mildly depleted in the ISM and varies between 0 and 0.3 dex in both short and long sightlines in the MW and in the SMC (Kimura et al. 2003; Jenkins 2009; Jenkins & Wallerstein 2017). Jenkins (2009) introduced a line-of-sight depletion factor F_*, which represents how far depletion has progressed collectively for all elements along a sightline, such that a larger F_* implies a stronger depletion for all elements. Although measuring S abundances was less straightforward than for other species, Jenkins' results indicate that the O/S ratio varies from −0.15 to +0.4 dex for $F_* =$ 0–1.0. For very dense interstellar clouds, depletion may be far more extreme (e.g., Ruffle et al. 1999), but for diffuse clouds with only small amounts of dust ($F_* \lesssim 0.5$), using S/H to measure O/H is likely a reasonable assumption.

In addition, S II is not only expected to be the dominant sulfur ion in neutral gas with N(H I) as high as that seen toward UGC 5282, but any ionization correction necessary to calculate N(S) is expected to be negligible. This is not only true for gas ionized by the extragalactic UV flux (e.g., Bowen et al. 2005)

but also for ionization by H II regions (e.g., James et al. 2014). The same arguments also apply to P II, which we discuss below.

If we therefore assume that all of the sulfur is in the form of S II, and that S is undepleted, then (S/H) = (S II/H I), and the metallicity Z of the neutral gas in UGC 5282 is

$$Z_{\rm H\,I}({\rm S}) = \left[\frac{\rm S}{\rm H}\right] \equiv \log\left(\frac{\rm S}{\rm H}\right) - \log\left(\frac{\rm S}{\rm H}\right)_\odot = -0.82\,(+0.39, -0.26)$$

where $12 + \log({\rm S/H})_\odot = 7.26 \pm 0.04$ is the protosolar value from Lodders (2003).

P is another element that is assumed to track O and S. Although P is not an α-element, it is thought to be produced in the same massive stars that produce O and S (Cescutti et al. 2012), and so it follows the α-elements as they are dispersed by type II SNae. In the Milky Way, P and S are depleted by very similar amounts as F_* varies (Jenkins 2009). We measure

$$Z_{\rm H\,I}({\rm P}) = \left[\frac{\rm P}{\rm H}\right] = -0.78\,(+0.30, -0.32),$$

again, assuming no depletion and no ionization corrections, and using $12 + \log({\rm P/H})_\odot = 5.54 \pm 0.04$ as the solar value.

The metallicities of S and P derived are sufficiently similar within their errors that we can take a simple weighted average of the two values to give a final estimate of the metallicity:

$$Z_{\rm H\,I}({\rm S, P}) \simeq -0.80 \pm 0.24,$$

i.e., 0.16 ± 0.09 times, or $\approx 1/6$ of, the solar value.

Finally, our measurements of Fe give an indication of the depletion Δ in the gas, since iron is known to be strongly depleted in diffuse clouds. If (Fe II/H I) is a good measure of Fe/H, then

$$\Delta({\rm Fe}) = [{\rm Fe/H}] - Z_{\rm H\,I}({\rm S, O}) = -0.61 \pm 0.42.$$

This value is much smaller than the depletion of Fe relative to S in the MW and the LMC—for all values of F_*—but is entirely consistent with the depletions found in DLAs at higher redshift (e.g., Kulkarni et al. 2015).

4.4. Consistency Checks

The spectrum of J0951+3307 contains several other absorption lines from UGC 5282 that are less suitable for abundance determinations, as they are either saturated or blended with unrelated features. However, we can check whether the model constructed for the weak lines shown in Figure 5 and listed in Table 3 can successfully predict the profiles of these other lines.

For example, the top panel of Figure 6 shows the S II λ1250 absorption arising from UGC 5282. This line was not used to constrain any column densities or b-values as the line is contaminated by H I λ930 at $z = 0.35080$. In this system, Lyβ, Lyγ, and Lyδ are all detected in the COS spectrum, enabling us to calculate the expected profile for the λ930 line at the position of the S II line. We find $\log N({\rm H\,I}) = 15.55 \pm 0.07$ and $b = 37.4 \pm 3.9$ km s^{-1} for this high-z system. The profile is shown as a green line in the figure. The S II λ1250 line itself can be predicted using the values of b, v, and N(S II) derived from the S II λ1259 line (Table 3), and this is shown as a red line in Figure 6. The blend of the two is shown in blue, and the results appears to agree well with the data.

The middle panel of Figure 6 shows the O I λ1302 absorption from UGC 5282. O I is an important species to observe, because O shows much less depletion as a function of F_* than S or P, and the ionization corrections needed to convert from O I to O are negligible, since charge exchange locks the ionization of oxygen to that of hydrogen (Field & Steigman 1971). The O I λ1302 absorption from UGC 5282 is saturated and very insensitive to the value of N(O I), but if we assume that there must exist a component with the same b and v values as the weak lines listed in Table 3, then we find that the line must be comprised of at least two components and that with b and v fixed for the DLA component (labeled "2" in the figure), a best fit can be computed. For completeness, the resulting values are listed in Table 3; the errors on N(O I) and, hence, on the metallicity are large, but the value of Z(O) is at least consistent with the values of $Z_{\rm HI}$(S) and $Z_{\rm HI}$(P). Figure 6 also shows the predicted line profile of component 2 for the same fixed values of b and v but with N(O I) derived from the same metallicity as inferred for sulfur, $Z_{\rm HI}({\rm S}) = -0.80$. This is shown as a cyan line in the figure; it is barely distinguishable from the best fit for component 2, which is 0.3 dex larger in column density. This demonstrates how insensitive the O I λ1302 is for measuring N(O I) but also that a simple two-component model with a priori knowledge of some of the fitting parameters can at least reproduce the data.

4.5. Lyα Emission from UGC 5282

Lyα is detected in emission at the bottom of the damped Lyα absorption line (Figure 7). The emission is clearly redward of the absorption lines seen toward J0951+3307, as well as the systemic velocity of UGC 5282 measured from 21 cm emission lines. The flux integrated over a Gaussian line fit is $(5.2 \pm 0.3) \times 10^{-17}$ erg cm^{-2} s^{-1} Å^{-1}, centered at 1706 km s^{-1} with a width of $\sigma = 108$ km s^{-1}. The corresponding luminosity is $(3.0 \pm 0.2) \times 10^{36}$ erg s^{-1}, although this only represents the amount seen through the COS aperture. There may also be emission blueward of the galaxy's systemic velocity (~900–1200 km s^{-1}); however, this may be directly related to the flux from the red wing of the wide geocoronal Lyα emission (see Figure 4), which makes it difficult to claim that the emission is real. The positive offset in velocity of the emission from UGC 5282 might suggest that either the emitting gas lies between us and the galaxy and is falling into it, or else the gas is outflowing from the other side of galaxy. Unfortunately, neither scenario is supported by the detection of any high-velocity absorption components.

Alternatively, the emission could be a radiative transfer effect due to resonant scattering of the Lyα line from the galaxy's ISM. The offset in the Lyα velocity is, for example, reminiscent of that seen in nearby galaxies (e.g., Hayes 2015; Orlitová et al. 2018, and references therein). In this case, the Lyα emission characteristics could have implications regarding the escape of Lyman continuum emission from the galaxy (e.g., Dijkstra et al. 2016) and feedback effects (e.g., McKinney et al. 2019). The low S/N of our data and the likely presence of geocoronal Lyα contamination at lower velocities preclude a detailed analysis of these issues, but higher S/N follow-up observations and mapping of the global Lyα emission from UGC 5282 could provide valuable insights on these topics.

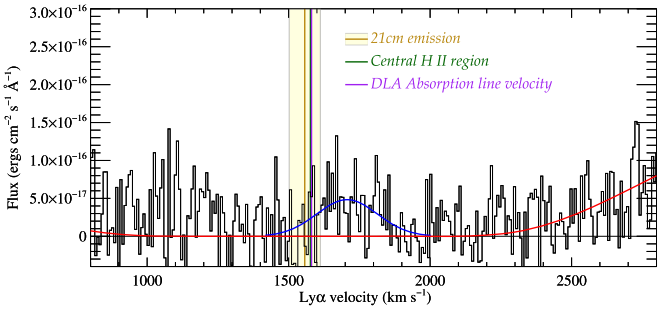

Figure 7. Comparison of Lyα emission toward J0951+3307 with three estimates of the velocity of UGC 5282. The yellow region shows the 21 cm emission tabulated by Schneider et al. (1990) with a width equivalent to $W_{50} = 110$ km s^{-1}, the width of the H I profile at 50% of its peak. The redshift of the central H II measured by SDSS is shown in green, and the velocity of the DLA component at 1581 km s^{-1} is shown in purple. The red line indicates the Lyα absorption profile. Although we consider the emission at 1706 km s^{-1} to be real, an apparent excess of flux between 900 and 1200 km s^{-1} may be due to contamination from geocoronal Lyα emission.

5. Differences in $Z_{\rm H\,I}$ and $Z_{\rm H\,II}$ in UGC 5282 and Other Star-forming Galaxies

With both $Z_{\rm H\,II}$ and $Z_{\rm H\,I}$ measured for UGC 5282, the difference between the two is simply

$$\delta({\rm X}) = Z({\rm X})_{\rm H\,II} - Z({\rm X})_{\rm H\,I}.$$

We take $Z_{\rm H\,II}({\rm O}) = -0.37 \pm 0.10$ from Table 2 (the S23 strong-line calibration and assuming an error of 0.10 in the calibration) and $Z_{\rm H\,I}({\rm P,\ S}) = -0.80 \pm 0.24$; this gives

$$\delta({\rm P,\ S}) = 0.43 \pm 0.26,$$

a value that indicates that the H II region abundances are a factor of $\sim$3 higher than those in the outer diffuse ISM.

How robust are the column densities listed in Table 3 and the resulting value of $Z({\rm X})_{\rm H\,I}$? Uncertainties arising from the modest S/N of our data are largely reflected in the large uncertainties attached to the measurements. In addition, the leverage that the available lines provide to measure column densities independent of their b values is not strong: if lines are unresolved, column densities are only robust for sets of lines with different transition probabilities, and for the spectrum of J0951+3307, we only have two lines of the S II λ1256 triplet available, one of which is contaminated by an intervening H I line at a higher redshift. This makes the model constructed for the absorption more uncertain.

One simple test of whether δ(P,S) is really different from zero is to re-fit the absorption lines assuming that they have the *same* metallicity as the gas in the H II region. With v and N fixed for the S II and P II lines, we find that the same lines shown in Figure 5 can be best fit with a single component that has $b = 10.9$ km s^{-1}. However, not only is χ^2 worse for the fits with these assumed column densities, but both the S II λ1259 and P II λ1152 lines seem too strong compared to the data. The bottom panel of Figure 6 shows the difference for the S II λ1250 line. The figure demonstrates that although the difference is small, the better fit to the data is still that seen in the top panel, which gives the values of N(S II) and b listed in Table 3 and the lower value of $Z({\rm P,\ S})_{\rm H\,I}$. While we caution that a definitive model for the absorption is difficult to define with the current data, we assume that the value of δ(P,S) given above is a reasonable estimate.

In order to compare the values of δ(P, S) from UGC 5282 with sightlines to other extragalactic star-forming regions, we compiled a list of low-z galaxies where both emission and absorption lines have been measured toward individual star clusters. The galaxies selected are shown in Table 4. We only included sightlines where $\log N({\rm H\,I}) > 20.1$ in the neutral gas absorption, in order to remove uncertainties from unknown ionization corrections in converting N(S) and N(P) from N(S II) and N(P II).

A significant problem in compiling these data, however, is knowing which published value of O/H should be used in calculating $Z_{\rm H\,II}$ for any particular galaxy. There are multiple ways to measure O/H from emission lines; in particular, abundances determined from RL methods are known to be 0.2 − 0.3 dex higher than those measured from the T_e method, while the former method agrees better with the metallicities of individual stars associated with H II regions (e.g., López-Sánchez et al. 2012, and references therein). Many of the published values of O/H for our selected galaxies were constructed using the T_e method, values of which may be inappropriate for UGC 5282, whose metallicity was measured using SEL methods (Table 2). To provide a fair comparison therefore, we calculated new SEL values of log O/H for our set of galaxies using the same indices we used for UGC 5282, namely Ar3O3, N2, O3N2, and KK04. To do this, we used the tables of emission-line intensities provided in the published papers listed at the end of Table 4. In most cases, we used line intensities that were already corrected for dust absorption and underlying Balmer absorption by the authors; although these corrections may have been made using, e.g., different extinction laws or R_V values, the differences are small in the optical for star-forming galaxies, and as we discuss below, they are insignificant compared to the systematic calibration errors in the metallicities derived from emission-line ratios. Four of the selected galaxies also had SDSS spectra available, which enabled us to measure $Z_{\rm H\,II}$ in exactly the same way as we did for UGC 5282, following the same analysis described in Section 3.

For the galaxies listed in Table 4, many authors report line intensities for multiple positions within a galaxy. We discuss in Section 6 what is currently known about the variations in $Z_{\rm H\,II}$ with position for these types of star-forming dwarf galaxies. But in order to avoid any errors that might arise from spatial variations in emission-line metallicity, we only included data if they were obtained at the same position as the apertures used for the absorption-line measurements. In most cases, the regions selected for both absorption and emission-line measurements were simply the brightest region of a galaxy, usually at its center. Similarly, for the new measurements made from existing SDSS spectra, in three of the four cases, the spectroscopic fibers appear to have been positioned on the same regions used to record the emission lines. For emission-line measurements published several decades ago, no information is given on the exact positions of the slits used, and we assume that the observations were made of the brightest regions of a galaxy. In these cases, we list in column 4 of Table 4 an indication of the spatial scale of the spectroscopic observations, if given by the authors. We list the emission-line-ratio metallicities measured at any and all positions within the absorption-line aperture in columns 5–8 of Table 4, in order to show the possible variations in log(O/H) that exist along the same sightlines where absorption-line metallicities are measured.

Table 4
Emission and Absorption-line Metallicities from Individual Galaxies

ID	Galaxy	H II Reference	H II Aper.	H II Metallicities				H I Reference	H I Aper.	H I Metallicities		
				Ar3O3	N2	O3N2	KK04			$Z_{H\,I}(O)$	$Z_{H\,I}(S)$	$Z_{H\,I}(P)$
(1)	(2)	(3)	(4)	(5)	(6)	(7)	(8)	(9)	(10)	(11)	(12)	(13)
1	SBS 0335−052 E	1	Nos. 4 + 5 FORS	7.15	7.61	7.91	7.65	2	COS	−3.69(± 0.07)	−2.00(± 0.07)	−2.27(± 0.16)
		1	Nos. 4 + 5 UVES	6.98	7.59	7.89	7.72					
		3	3.″5	7.00	7.54	7.87	7.68					
2	I Zw18 NW	4	3″	7.47	7.63	7.95	⋯	2,5	COS	−1.69(± 0.06)	−1.83(± 0.08)	−1.92(± 0.31)
		6	NW-knot	7.55	7.58	7.93	7.63					
		3	3.″5	7.53	7.47	7.88	⋯					
		7	P0-B0	7.74	7.58	7.94	7.60					
		7	P0-C0	7.53	7.59	7.93	7.56					
3	I Zw 36	4	3″	7.72	7.77	7.91	⋯	8	LWRS	$-1.26\,(^{+1.85}_{-1.02})$	...	$-1.84\,(^{+0.30}_{-0.38})$
		3	3.″5	7.75	⋯	⋯	8.18					
4	SBS 1415 + 437	9	n/a	7.84	7.87	8.01	8.04	2	COS	−2.98 (±0.11)	−1.39 (±0.05)	−1.20 (±0.09)
		10	e1	7.83	7.86	8.00	7.99					
		11	5″	7.78	7.88	8.01	8.02					
		11	0.″6	7.75	7.83	7.99	7.99					
5	NGC 1705	12	s7-1	8.17	8.10	8.13	8.22	13	LWRS	−1.33 (±0.22)	⋯	⋯
		12	s7-2	8.10	8.08	8.10	8.27					
		12	s8-1	8.05	8.04	8.07	8.19					
		12	s8-2	8.06	8.07	8.09	8.20					
		12	s8-3	8.08	8.12	8.12	8.26					
		12	s8-4	8.13	8.19	8.17	8.28					
6	Pox 36	14	5.″5	8.13	8.08	8.10	8.35	15	LWRS	−1.52(± 0.13)	⋯	−0.88(± 0.18)
		16	4″	⋯	8.10	8.10	8.37					
7	NGC 4670	4	3″	8.26	8.19	8.17	⋯	2	COS	−2.57(± 0.10)	−0.73(± 0.09)	−0.79(± 0.10)
		17	Region 1	⋯	8.14	8.12	8.15					
8	NGC 5253−1[a]	18	UV2	8.31	8.23	8.19	8.36	2	COS	−2.52(± 0.15)	−1.02(± 0.05)	−1.00(± 0.09)
9	NGC 604	19	6″	8.36	8.27	8.25	7.88	20	Various	−1.21(± 0.30)	⋯	−0.59(± 0.32)
		21	n/a	8.45	8.33	8.27	8.08					
10	NGC 3690[a]	4	3″	8.42	8.56	8.44	⋯	2	COS	−1.90(± 0.06)	−0.46(± 0.06)	⋯
11	NGC 4214	22	n/a	⋯	8.25	8.20	8.45	2	COS	−2.63(± 0.06)	−0.82(± 0.06)	−0.90(± 0.06)
12	NGC 4449	23	main reg.	⋯	8.37	8.29	8.33	2	COS	−2.36(± 0.06)	−0.79(± 0.10)	−0.57(± 0.10)
		22	n/a	⋯	8.31	8.27	8.31					

Table 4
(Continued)

ID	Galaxy	H II Reference	H II Aper.	H II Metallicities Ar3O3	N2	O3N2	KK04	H I Reference	H I Aper.	H I Metallicities $Z_{\rm H\,I}$(O)	$Z_{\rm H\,I}$(S)	$Z_{\rm H\,I}$(P)
(1)	(2)	(3)	(4)	(5)	(6)	(7)	(8)	(9)	(10)	(11)	(12)	(13)
13	NGC 625	24	No. 5	⋯	8.11	8.10	8.26	25	MDRS	$-1.46(\pm0.33)$	⋯	$-0.50(\pm0.34)$
		24	No. 9	⋯	8.21	8.19	8.19					
		24	No. 18	⋯	8.27	8.23	7.69					
						QSOs behind galaxies						
14	SBS 1543+ 5921+ HS 1543+ 593	26	n/a	⋯	8.18	8.15	8.34	27	STIS	⋯	$-0.49(\pm0.08)$	⋯
15	UGC 5282+ Q0951+ 3307	4	2″	8.43	8.26	8.27	8.36	4	COS	⋯	$-0.82\ (^{+0.39}_{-0.26})$	$-0.78\ (^{+0.30}_{-0.32})$

Notes. Columns (1): These numbers are used to identify galaxies in Figure 8; (2): galaxy name; (3): reference to the work used herein to measure H II emission-line ratios (see reference list below); (4): name of the aperture used by the authors in column 3, quoted verbatim if available, or, approximate size of aperture used to obtain emission-line data; (5–8): values of 12+log(O/H) metallicities derived from the emission-line ratios. Values of O3N2 are included for completeness, even though it has already been established that many of the listed galaxies have such low metallicities that the O3N2 parameter is invalid in these cases; (9): reference to the work used to measure absorption lines (see below); (10): instrument aperture used to measure absorption lines. All COS observations used the 2.″5 diameter Primary Science Aperture (PSA); the designations "LWRS" and "MDRS" refer to the 30 × 30″ and 4.0 × 20″ apertures of the FUSE satellite, respectively. The *Space Telescope Imaging Spectrograph* (STIS) observations of HS 1543+593 were made with the 52 × 0.″1 aperture; (11–13): metallicities $Z_{\rm H\,I}$ derived from absorption lines assuming solar abundances.

[a] For NGC 3690, there may be a mismatch in the position of the absorption and emission-line apertures: the position of the SDSS fiber used to measure the emission lines is recorded as being ≈13″ from the UV source used by James et al. (2014) to measure absorption lines. For NGC 5253, the position of "NGC 5253−2" listed in James et al. (2014) does not correspond to the position of "Aperture 2" (or "UV4") labeled by Calzetti et al. (1997) and so is not included in this list.

References. (1) Izotov et al. (2009), (2) James et al. (2014), (3) Izotov et al. (1997), (4) this paper; (5) Lebouteiller et al. (2013) (6) Kehrig et al. (2016), (7) Vilchez & Iglesias Páramo (1998), (8) Lebouteiller et al. (2004), (9) Melbourne et al. (2004), (10) Guseva et al. (2003), (11) Thuan et al. (1999), (12) Annibali et al. (2015), (13) Heckman et al. (2001), (14) Izotov & Thuan (2004), (15) Lebouteiller et al. (2009), (16) Kunth & Sargent (1983), (17) Kumari et al. (2018), (18) López-Sánchez et al. (2007), (19) Esteban et al. (2009), (20) Lebouteiller et al. (2006), (21) Vilchez et al. (1988), (22) Kobulnicky et al. (1999), (23) Kumari et al. (2017), (24) Skillman et al. (2003), (25) Cannon et al. (2005), (26) Schulte-Ladbeck et al. (2005), (27) Bowen et al. (2005). In this paper (Ref "4" in column 3), the following SDSS spectra were used: I Zw 18 NW—0555-52266-0558; I Zw 36—1453-53084-0322; NGC 4670—2238-54205-0222; NGC 3690—0952-52409-0247.

For the absorption-line measurements, $Z_{\rm H\,I}$(O), $Z_{\rm H\,I}$(S), and $Z_{\rm H\,I}$(P) were calculated from the published column densities and using the same solar abundance used for UGC 5282. These are listed in columns 11–13 of Table 4. In calculating δ, we favored $Z_{\rm H\,I}$(S) over $Z_{\rm H\,I}$(P), and used $Z_{\rm H\,I}$(O) only once (NGC 1705) where no S II or P II lines had been measured. The large differences in $Z_{\rm H\,I}$(O) compared to $Z_{\rm H\,I}$(S) and $Z_{\rm H\,I}$(P) seen toward several objects almost certainly arise from the fact that a single, likely saturated O I absorption line was used.

Values of δ are shown in Figure 8, where δ for an individual object is the mean of the values listed for that object in Table 4. The figure excludes the values of δ from the O3N2 method, since the index is known to break down for metallicities below 12+log(O/H) $\lesssim$ 8.3 (Pettini & Pagel 2004; Marino et al. 2013), and all of the galaxies in Table 4 have O3N2 less than this limit. For the other indices, the dominant contribution to the errors in δ is that from the absolute calibration of Ar3O3, N2, and KK04, and we take a conservative approach and simply use the same values of $\sigma_{\rm SL}$ listed in column 3 of Table 2 as the error in $Z_{\rm H\,II}$ for each object. That is, we plot $\delta = (\langle Z_{\rm H\,II}\rangle - Z_{\rm H\,I}) \pm \sigma_{\rm SL}$ for each galaxy. These errors are significantly larger than the errors in individual emission-line measurements, as well as the resulting errors in the emission-line ratios, and are larger than most of the errors in $Z_{\rm H\,I}$(X); the latter are still added in quadrature to the former, however.

Also plotted in Figure 8 are the values of δ for the two dwarf galaxies that are probed by QSO sightlines, SBS 1543+5921, and our new results for UGC 5282. The value of δ for UGC 5282 is higher than that seen toward SBS 1543+5921, although their errors clearly overlap. Both values of δ are similar to the ensemble of δ values for the star-forming galaxies. Weighted averages for all of the sightlines are shown as dashed lines in the figure and are of a similar value, $\langle\delta\rangle$ = 0.4–0.5. This is a factor of two higher than the value of $\langle\delta\rangle = 0.20 \pm 0.23$, found by James & Aloisi (2018) using a smaller number of sightlines. The difference between our value and theirs is within the range of systematic offsets found when different indices are used to measure emission-line metallicities.

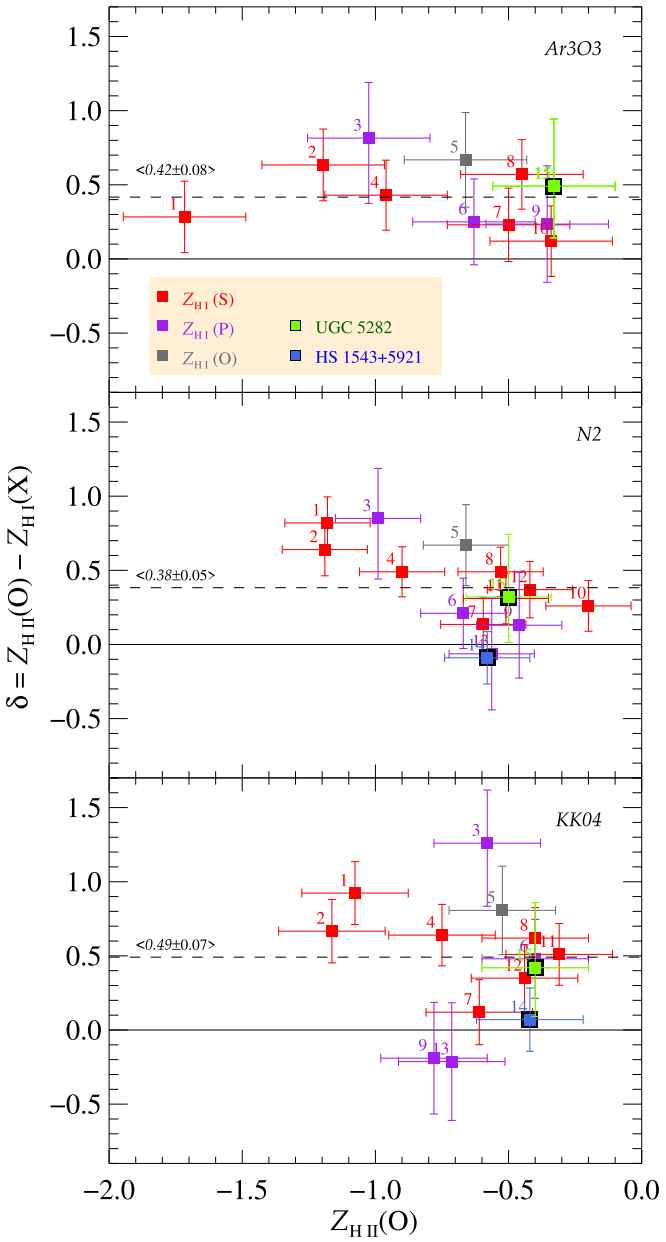

Figure 8. Plots showing the difference in metallicities δ between ionized gas ($Z_{\rm H\,II}$) measured from emission lines from H II regions and neutral gas ($Z_{\rm H\,I}$) measured by absorption lines toward the H II regions, or, in two cases, background QSOs. To the first order, $Z_{\rm H\,II}$ represents the metallicity of gas within or close to the H II region, while $Z_{\rm H\,I}$ measures the abundances of the ISM in the rest of the galaxy along the line of sight. $Z_{\rm H\,II}$ is measured using three different methods, the Ar3O3, N2, and KK04 strong emission-line ratios. Points are numbered with the IDs listed in column 1 of Table 4. The use of S II, P II, or, in a single case, O I absorption lines for measuring $Z_{\rm H\,I}$ are indicated by the use of red, purple, or gray squares, as described in the legend in the top panel. When measuring δ, $Z_{\rm H\,I}$(S) was preferred over $Z_{\rm H\,I}$(P), both of which were selected over $Z_{\rm H\,I}$(O). Values of δ for the two QSOs intercepting foreground galaxies are also indicated. The dashed horizontal lines indicate weighted averages of all of the values of δ. For each panel, the error bars are a quadratic sum of the errors in the column densities from measuring $Z_{\rm H\,I}$, and the systematic calibration errors in determining $Z_{\rm H\,II}$ given by $\sigma_{\rm SL}$ in Table 2.

6. Discussion

The values of δ shown in Figure 8 suggest that a real difference exists between the metallicity of the ionized ISM in which stars are forming ($Z_{\rm H\,II}$) and the metallicity of the neutral ISM that constitutes the galaxy ($Z_{\rm H\,I}$). The suggestion that δ is greater than zero toward H II sources in nearby starburst galaxies is not new (e.g., Cannon et al. 2005; Lebouteiller et al. 2013; James & Aloisi 2018), but the sightline to J0951+3307 measures the bulk of UGC 5282's ISM metallicity ~1 kpc *away* from the brightest regions of star formation and along a sightline through the *entire* galaxy. If a nonzero value of δ is a common feature in low-mass galaxies, then our result may indicate that there exists a "baseline" galaxy metallicity that is better measured from its cool neutral ISM. The true "metallicity" of a galaxy is not that measured from $Z_{\rm H\,II}$ but from $Z_{\rm H\,I}$.

Why should $Z_{\rm H\,I}$ and $Z_{\rm H\,II}$ be different? Star-forming regions certainly add metals to the ISM, but the metallicity measured is that of gas enriched from earlier episodes of star formation and not from the bursts that are marked by the H II regions we observe. The H II regions that are currently active are ejecting material through supernovae or stellar winds, and much of the gas that contains the newly made metals is expected to be hot, at temperatures of 10^{6-8} K, at least for a few hundred Myr (Emerick et al. 2019). The temperature of the gas from which $Z_{\rm H\,II}$ is measured now is less than this, 10^{4-5} K (e.g.,

Kewley et al. 2019), and new metal-rich gas contributes little to the optical-line emission used to measure $Z_{\rm H\,II}$. Evidence for the hot gas can be found in its X-ray emission (McQuinn et al. 2018, and references therein) and in O VI absorption in the FUV (Grimes et al. 2009). Thus the "enriched" material whose metallicity is measured by $Z_{\rm H\,II}$ is gas that was once hot but has cooled and been able to return to the ISM and is now ionized by nearby stars. This re-enrichment of the ISM may not be particularly efficient; the outflows remain hot for at least the lifetime of the H II regions, several tens of Myr (Legrand et al. 2001), and may be sustained over the lifetime of the starburst activity, perhaps as much as several hundred Myr (McQuinn et al. 2018). Complete recycling of gas may take up to a Gyr (Christensen et al. 2016). In addition, metals may be lost to the IGM because of the low gravitational potential of the dwarf galaxy (e.g., Mac Low & Ferrara 1999; Ferrara & Tolstoy 2000; McQuinn et al. 2015; Emerick et al. 2018); although, how much material (in either mass or metals) escapes remains unclear (Muratov et al. 2017; McQuinn et al. 2019).

Although the exact details of how gas cools and remixes with the ISM are complex, the enrichment is likely to be spread over the size of the outflows, i.e., over kiloparsec scales. Indeed, there is good evidence for a well-mixed ISM in low-mass galaxies. The most recent observations using multiple spectroscopic slits or integral field spectrographs suggest that on kiloparsec scales, gas metallicity is quite homogeneous, with either no obvious variations in $Z_{\rm H\,II}$ between sources (e.g., Lagos et al. 2012, 2016; Kehrig et al. 2016; Cairós & González-Pérez 2017) or only small perturbations characterized by weak metallicity gradients (e.g., Annibali et al. 2019, 2017, 2015; Bresolin 2019, and references therein). Consequently, even if UGC 5282 had a metallicity gradient similar to other low-mass galaxies, the difference in $Z_{\rm H\,II}$ over the 1 kpc distance between the center of UGC 5282 and the sightline to J0951+3307 ought to be negligible if gas is well mixed.

Moreover, if mixing is effective over kiloparsec scales, then we would expect the neutral gas observed toward the QSO and the ionized gas seen toward the central H II region to have the same metallicity. In which case, in order to find $Z_{\rm H\,I} < Z_{\rm H\,II}$, a significant fraction of the neutral gas must be many kiloparsecs away from the star-forming regions in order to not be contaminated. Such an explanation was adopted by Cannon et al. (2005), who postulated the existence of a low-metallicity halo beyond the inner ISM to explain the discrepancy between $Z_{\rm H\,I}$ and $Z_{\rm H\,II}$ toward star-forming regions in NGC 625. Our results are consistent with this idea and provide additional evidence for IGM gas feeding into galaxies through streams from the cosmic web (e.g., Sánchez Almeida et al. 2014a, and references therein). Dwarf galaxy *pairs* in particular are thought to have enhanced star formation because they are fed by significant reservoirs of neutral gas in which they reside, or because of their mutual interactions (Lelli et al. 2014; Stierwalt et al. 2015; Pearson et al. 2016). As noted in Section 2.4, UGC 5282 does lie near a galaxy of similar mass (UGC 5287 in Figure 3) and interactions between the two galaxies may be the source of gas flowing into UGC 5282. For example, Pearson et al. (2018) have suggested that multiple encounters between dwarf galaxies can "park" gas at significant distances from the protagonists, which can then return over several Gyr. It remains unknown whether the metallicity of such returning debris would be low enough to cause the decrease in metallicity in either UGC 5282 or UGC 5287, but it may reflect whatever buildup of metals occurred in the dwarfs at much earlier times. Alternative tidal models that cause strong metallicity gradients and the *removal* of low-metallicity gas at the edges of dwarf galaxies (Williamson et al. 2016) seem less well supported by our results. Indeed, the situation for UGC 5282 may be even more complicated, depending on whether it has entered the halo of NGC 3003 (Figure 3) and has begun to feel any effects from ram pressure stripping by gas in the host's halo. The effects on the metallicity of the dwarf galaxy may, however, be less significant than any effects from tidal stripping (Williamson & Martel 2018).

Although dwarf galaxies usually show a well-mixed ISM, there are exceptions. In particular, some dwarf galaxies demonstrate regions where $Z_{\rm H\,II}$ decreases significantly ($\sim$1 dex over only a few hundred parsecs) at positions of high star-formation surface density compared to $Z_{\rm H\,II}$ from the rest of the galaxy, $Z_{\rm host}$ (Richards et al. 2014; Sánchez Almeida et al. 2018, 2015, 2014b). This is again attributed to the influx of low-metallicity gas from the IGM that dilutes the ISM, but this time on subkiloparsec scales. These examples argue for much more local mixing of IGM gas with the ISM. $Z_{\rm H\,I}$ toward these specific regions of low $Z_{\rm H\,II}$ has not been measured, and whether $Z_{\rm H\,I}$ would be even lower than $Z_{\rm H\,II}$ is not known, and likely depends on the degree of mixing. In principle, a similar scenario might exist in UGC 5282, with the central H II region being the site of inflowing gas. This is hard to reconcile with our result that $Z_{\rm H\,I} < Z_{\rm H\,II}$ though; the inflow toward the H II region might occur on subkiloparsec scales, yet we see a lower metallicity along the QSO sightline a kiloparsec away, where there is—by definition in this model—less inflow. The obvious test of such local mixing for UGC 5282 would require a measurement of $Z_{\rm H\,I}$ toward the central H II region and a measurement of $Z_{\rm H\,II}$ toward the QSO line of sight: for only local mixing, $Z_{\rm H\,I}$ toward the H II region would be less than $Z_{\rm H\,I}$ toward the QSO as low-metallicity gas mixes with the ISM, while $Z_{\rm H\,II}$ toward the QSO would be higher than $Z_{\rm H\,II}$ toward the central H II region.

The difference in the baseline metallicity that is assumed for a galaxy can be important for understanding the evolution of galaxies. For example, in the canonical closed-box model of a galaxy, the metallicity can be expressed as a function of the gas mass fraction $[M_{\rm gas}/(M_{\rm gas} + M_{\rm stars})]$ and the yield (the ratio of the rate at which metals are ejected into the ISM to the rate at which hydrogen is removed by star formation (Searle & Sargent 1972)). Deviations of the measured metallicity of the gas compared to expected values are usually taken to indicate the presence of either inflowing or outflowing gas (e.g., Lagos et al. 2018, and references therein). A difference of $\sim$0.5 dex in the assumed "true" metallicity of the gas can change entirely whether a measured metallicity is consistent with flows of gas in or out of a galaxy.

In addition, our results may have more general consequences for the calibration of the well-known mass–metallicity relation, MZR, and the mass–metallicity–SFR correlation, M_*–Z–SFR (Hirschauer et al. 2018, and references therein). Galaxy evolution models attempt to reproduce the slope, shape, and scatter within these relationships (despite the difficulties in the absolute calibration of O/H discussed in Section 3). The position of UGC 5282 on the MZR diagram is shown in Figure 9, which, in this particular case, uses the results constructed by Andrews & Martini (2013). Both $Z_{\rm H\,I}$ and $Z_{\rm H\,II}$

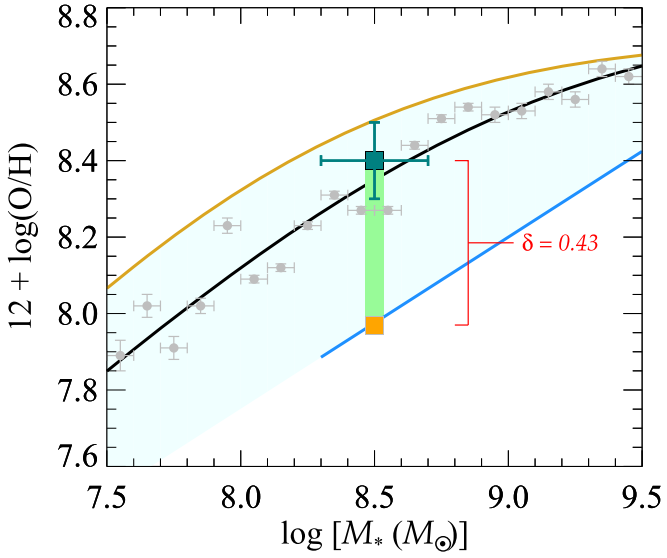

Figure 9. Comparison of the metallicity $Z_{\rm H\,II}$ and stellar mass of UGC 5282 to the stellar mass–metallicity–SFR (M_*–Z–SFR) relationship for 200,000 SDSS galaxies studied by Andrews & Martini (2013). The black line represents the M_*–Z–SFR relation found without considering the SFR of the sample galaxies. The gray circles show the data used to produce the black line and are included to indicate the dispersion in the data. The yellow and blue lines show the resulting M_*–Z–SFR relations when the galaxies are binned into a sample with low SFRs, $-1.0 \leqslant \log(\mathrm{SFR}) < -0.5$, and with high SFRs, $0.5 \leqslant \log(\mathrm{SFR}) < 1.0$, respectively. The green square shows the position of $Z_{\rm H\,II}$ for UGC 5282, while the orange square shows the value of $Z_{\rm H\,I}$. The difference between the two, the value of δ discussed in this paper, is of the same magnitude as the M_*–Z–SFR purports to measure for different SFRs. This suggests that the baseline metallicity of a galaxy should be that of the neutral ISM, as it may be significantly different than the emission-line metallicities that define the M_*–Z–SFR relationship.

found in UGC 5282 are plotted. The difference between the two is of a magnitude similar to the difference between the full range of correlations that exist for different ranges of the SFRs, from $-1.0 \leqslant \log(\mathrm{SFR}) \leqslant 1.0$. This suggests that positive values of δ of the magnitude discussed in this paper could be an important factor in the calibration of the M_*–Z–SFR relation and also that models and numerical simulations that attempt to explain this important correlation ought to start with a lower baseline metallicity for galaxies than those that currently employ $Z_{\rm H\,II}$.

As yet, we do not know if positive values of δ exist for much more massive galaxies. Some absorption-line measurements of gas outside of the local ISM (along sightlines toward background QSOs) support the idea of infalling low-metallicity gas (Ribaudo et al. 2011) and even show evidence of the mixing of outflowing and inflowing material in their CGM (Frye et al. 2019). At distances of many tens of kiloparsecs, there appears to be significant offsets in $Z_{\rm H\,II}$ and the metallicity of the CGM (Kacprzak et al. 2019). Within higher-mass late-type galaxies, star-formation processes are clearly modified by factors not experienced by dwarf galaxies, such as the density waves that define the former's spiral structure. Strong negative metallicity gradients clearly demonstrate that the metallicity of ionized gas ($Z_{\rm H\,II}$) changes with galactocentric radius, and there is some evidence that there are local variations imprinted on the radial gradients that may be due to inflows from the IGM (Howk et al. 2018; Hwang et al. 2019) or mixing-induced dilution of the metals by the spiral density waves passing through the disk (Ho et al. 2017). These ideas can eventually be tested by measuring $Z_{\rm H\,I}$ toward multiple H II sites in large local disk-galaxies and by mapping variations in both $Z_{\rm H\,I}$ and δ over kiloparsec and subkiloparsec scale lengths.

7. Summary

We summarize the results of this paper as follows:

1. We have used COS to observe the QSO J0951+3307 behind the galaxy UGC 5282. The galaxy has a systemic redshift of $cz = 1577$ km s^{-1}, and has a luminosity, type, and H I gas mass similar to the SMC. Like the SMC, UGC 5282 is part of a group of galaxies, although it is further away from its more massive host than the SMC is from the Milky Way. The background QSO was selected specifically because of the identification of its sightline through the dwarf galaxy, and does not represent an unbiased probe of N(H I) in the local universe. We have used the emission lines in an SDSS spectrum of the central H II region to derive a metallicity of $Z_{\rm H\,II} = -0.37 \pm 0.10$ in the ionized gas using the S23 strong-line ratio, although a selection of other methods produce metallicities that agree well with this value.
2. The COS spectrum shows that at a galactocentric radius of $\simeq$1 kpc, UGC 5282 is a DLA absorber, with log N(H I) = 20.89 [+0.12, −0.21] at a redshift of $cz = 1581$ km s^{-1}. Metal lines are detected from the DLA, and the analysis of a set of weak lines suggests that the metallicity of the neutral gas (assuming no depletion from dust and no need of any ionization corrections) is $Z_{\rm H\,I} = -0.80 \pm 0.24$, which is lower than that seen in the ionized H II region gas by a factor of $\sim$3.
3. The difference in the metallicity seen in absorption and that in emission, δ, is higher ($\approx$0.4 dex) than the value found along a previous QSO sightline that intercepted the dwarf galaxy SBS 1543+5921, although their errors overlap. UGC 5282 has a value of δ similar to those measured toward bright H II regions within a set of dwarf star-forming galaxies. Although the errors toward individual sightlines are often large, we confirm that collectively, a small offset of $\delta \approx$ 0.4–0.5 dex persists in the data.
4. If the evolution of UGC 5282 is such that the metals throughout the galaxy have been well mixed on kiloparsec scales, then the simplest model to explain the fact that $Z_{\rm H\,I} < Z_{\rm H\,II}$ is that low-metallicity gas from the IGM has flowed into the galaxy and diluted the gas in the ISM, leading to a low value of $Z_{\rm H\,I}$ along the line of sight to the QSO. This model is consistent with the detection of Lyα emission in the core of the damped Lyα profile at a velocity offset from the galaxy's systemic velocity.

UGC 5282 remains a largely unstudied galaxy, and some obvious additional observations would help elucidate the origin of the DLA better. High spatial resolution 21 cm maps of the distribution of high N(H I) would show how strongly the galaxy is interacting with its environment, through, e.g., its morphological asymmetry, the presence of tidal features, additional H I companions closer than UGC 5287, etc. Integral field spectroscopy of the emission lines across the galaxy is now possible with modern instruments and would test whether $Z_{\rm H\,II}$ changes between the central H II region and the QSO sightlines or whether there exists dramatic discontinuities in $Z_{\rm H\,II}$ as a result of strong inflows from the IGM. Finally, ground-based, high-S/N echelle observations of Ti II in the spectrum of

J0951+3307 would better constrain the absorption-line model measured in the UV data and could provide an additional estimate of the metallicity and dust depletion of the neutral gas along the sightline.

The work required to identify QSOs behind galaxies was supported by a NASA *Long Term Space Astrophysics* (LTSA) grant NNG05GE26G. Funding for the reduction of the COS spectra obtained from the GO program was provided by NASA grant number 12486 from the Space Telescope Science Institute (STScI), which is operated by the Association of Universities for Research in Astronomy, Inc. (AURA), under NASA contract NAS5-26555. Funding for *Sloan Digital Sky Survey* SDSS-III has been provided by the Alfred P. Sloan Foundation, the Participating Institutions, the National Science Foundation (NSF), and the U.S. Department of Energy Office of Science. CALCOS and PyRAF are products of the STScI, which is operated by AURA for NASA. IRAF, on which parts of PyRAF are based, is distributed by the National Optical Astronomy Observatory, which is operated by AURA under a cooperative agreement with the NSF. This publication makes use of data products from the WISE satellite, which is a joint project of the University of California, Los Angeles, and the Jet Propulsion Laboratory/California Institute of Technology, funded by NASA. The STARLIGHT project is supported by the Brazilian agencies CNPq, CAPES, and FAPESP and by the France-Brazil CAPES/Cofecub program. This research has made use of the NASA/IPAC Extragalactic Database (NED), which is operated by the Jet Propulsion Laboratory, California Institute of Technology, under contract with NASA.

Facilities: HST (COS), WISE, GALEX, ARC (SPIcam, DIS), SDSS.

ORCID iDs

David V. Bowen https://orcid.org/0000-0002-5668-0397
Todd M. Tripp https://orcid.org/0000-0002-1218-640X
Edward B. Jenkins https://orcid.org/0000-0003-1892-4423
Renyue Cen https://orcid.org/0000-0001-8531-9536

References

Alloin, D., Collin-Souffrin, S., Joly, M., & Vigroux, L. 1979, A&A, 78, 200
Aloisi, A., Savaglio, S., Heckman, T. M., et al. 2003, ApJ, 595, 760
Amorín, R. O., Pérez-Montero, E., & Vilchez, J. M. 2010, ApJL, 715, L128
Andrews, B. H., & Martini, P. 2013, ApJ, 765, 140
Annibali, F., La Torre, V., Tosi, M., et al. 2019, MNRAS, 482, 3892
Annibali, F., Tosi, M., Pasquali, A., et al. 2015, AJ, 150, 143
Annibali, F., Tosi, M., Romano, D., et al. 2017, ApJ, 843, 20
Baldwin, J. A., Phillips, M. M., & Terlevich, R. 1981, PASP, 93, 5
Berg, D. A., Erb, D. K., Henry, R. B. C., Skillman, E. D., & McQuinn, K. B. W. 2019, ApJ, 874, 93
Berg, D. A., Skillman, E. D., Marble, A. R., et al. 2012, ApJ, 754, 98
Bowen, D. V., Chelouche, D., Jenkins, E. B., et al. 2016, ApJ, 826, 50
Bowen, D. V., Jenkins, E. B., Pettini, M., & Tripp, T. M. 2005, ApJ, 635, 880
Bowen, D. V., Jenkins, E. B., Tripp, T. M., et al. 2008, ApJ, 176, 59
Bresolin, F. 2019, MNRAS, 488, 3826
Brinchmann, J., Kunth, D., & Durret, F. 2008, A&A, 485, 657
Brown, M. S., Alkhayat, R. B., Irving, R. E., et al. 2018, ApJ, 868, 42
Brown, T., Catinella, B., Cortese, L., et al. 2017, MNRAS, 466, 1275
Cairós, L. M., & González-Pérez, J. N. 2017, A&A, 600, A125
Calzetti, D. 2013, in Secular Evolution of Galaxies, ed. J. Falcón-Barroso & J. H. Knapen (Cambridge: Cambridge Univ. Press), 419
Calzetti, D., Meurer, G. R., Bohlin, R. C., et al. 1997, AJ, 114, 1834
Cannon, J. M., Skillman, E. D., Sembach, K. R., & Bomans, D. J. 2005, ApJ, 618, 247
Cardelli, J. A., Clayton, G. C., & Mathis, J. S. 1989, ApJ, 345, 245
Cescutti, G., Matteucci, F., Caffau, E., & François, P. 2012, A&A, 540, A33
Christensen, C. R., Davé, R., Governato, F., et al. 2016, ApJ, 824, 57
Cid Fernandes, R., Mateus, A., Sodré, L., Stasinska, G., & Gomes, J. M. 2005, MNRAS, 358, 363
Dalcanton, J. J. 2007, ApJ, 658, 941
Dekel, A., & Birnboim, Y. 2006, MNRAS, 368, 2
Dekel, A., & Silk, J. 1986, ApJ, 303, 39
Díaz, A. I., & Pérez-Montero, E. 2000, MNRAS, 312, 130
Digby, R., Navarro, J. F., Fattahi, A., et al. 2018, MNRAS, 485, 5423
Dijkstra, M., Gronke, M., & Venkatesan, A. 2016, ApJ, 828, 71
El-Badry, K., Quataert, E., Wetzel, A., et al. 2017, MNRAS, 473, 1930
Emerick, A., Bryan, G. L., Low, M.-M. M., et al. 2018, ApJ, 869, 94
Emerick, A., Bryan, G. L., & Mac Low, M. M. 2019, MNRAS, 482, 1304
Emerick, A., Low, M.-M. M., Grcevich, J., & Gatto, A. 2016, ApJ, 826, 148
Esteban, C., Bresolin, F., Peimbert, M., et al. 2009, ApJ, 700, 654
Federman, S. R., Brown, M., Torok, S., et al. 2007, ApJ, 660, 919
Ferrara, A., & Tolstoy, E. 2000, MNRAS, 313, 291
Field, G. B., & Steigman, G. 1971, ApJ, 166, 59
Fillingham, S. P., Cooper, M. C., Pace, A. B., et al. 2016, MNRAS, 463, 1916
Frye, B. L., Bowen, D. V., Tripp, T. M., et al. 2019, ApJ, 872, 129
Gallart, C., Monelli, M., Mayer, L., et al. 2015, ApJL, 811, L18
Garnett, D. R. 2002, ApJ, 581, 1019
Geha, M., Blanton, M. R., Yan, R., & Tinker, J. L. 2012, ApJ, 757, 85
Gioannini, L., Matteucci, F., Vladilo, G., & Calura, F. 2017, MNRAS, 464, 985
Gordon, K. D., Clayton, G. C., Misselt, K. A., Landolt, A. U., & Wolff, M. J. 2003, ApJ, 594, 279
Green, J. C., Froning, C. S., Osterman, S., et al. 2012, ApJ, 744, 60
Grimes, J. P., Heckman, T., Aloisi, A., et al. 2009, ApJS, 181, 272
Guseva, N. G., Papaderos, P., Izotov, Y. I., et al. 2003, A&A, 407, 105
Hayes, M. 2015, PASA, 32, 27
Heckman, T. M., Sembach, K. R., Meurer, G. R., et al. 2001, ApJ, 554, 1021
Herrmann, K. A., Hunter, D. A., Zhang, H. X., & Elmegreen, B. G. 2016, AJ, 152, 177
Hirschauer, A. S., Salzer, J. J., Janowiecki, S., & Wegner, G. A. 2018, AJ, 155, 82
Hirschauer, A. S., Salzer, J. J., Skillman, E. D., et al. 2016, ApJ, 822, 108
Ho, I.-T., Seibert, M., Meidt, S. E., et al. 2017, ApJ, 846, 39
Howk, J. C., Rueff, K. M., Lehner, N., et al. 2018, ApJ, 856, 166
Hummer, D. G., & Storey, P. J. 1987, MNRAS, 224, 801
Hwang, H.-C., Barrera-Ballesteros, J. K., Heckman, T. M., et al. 2019, ApJ, 872, 144
Izotov, Y. I., Guseva, N. G., Fricke, K. J., & Papaderos, P. 2009, A&A, 503, 61
Izotov, Y. I., & Thuan, T. X. 2004, ApJ, 602, 200
Izotov, Y. I., Thuan, T. X., & Lipovetsky, V. A. 1997, ApJS, 108, 1
James, B., & Aloisi, A. 2018, ApJ, 853, 124
James, B. L., Aloisi, A., Heckman, T., Sohn, S. T., & Wolfe, M. A. 2014, ApJ, 795, 109
James, B. L., Koposov, S. E., Stark, D. P., et al. 2017, MNRAS, 465, 3977
Jedrzejewski, R. I. 1987, MNRAS, 226, 747
Jenkins, E. B. 2009, ApJ, 700, 1299
Jenkins, E. B., & Wallerstein, G. 2017, ApJ, 838, 85
Kacprzak, G. G., Pointon, S. K., Nielsen, N. M., et al. 2019, ApJ, 886, 91
Kalberla, P. M. W., Burton, W. B., Hartmann, D., et al. 2005, A&A, 440, 775
Kehrig, C., Vilchez, J. M., Pérez-Montero, E., et al. 2016, MNRAS, 459, 2992
Kereš, D., Katz, N., Weinberg, D. H., & Dave, R. 2005, MNRAS, 363, 2
Kewley, L. J., Nicholls, D. C., & Sutherland, R. S. 2019, ARA&A, 57, 511
Kimura, H., Mann, I., & Jessberger, E. K. 2003, ApJ, 582, 846
Kisielius, R., Kulkarni, V. P., Ferland, G. J., Bogdanovich, P., & Lykins, M. L. 2014, ApJ, 780, 76
Kobulnicky, H. A., Kennicutt, R. C., Jr., & Pizagno, J. L. 1999, ApJ, 514, 544
Kobulnicky, H. A., & Kewley, L. J. 2004, ApJ, 617, 240
Koppen, J., & Hensler, G. 2005, A&A, 434, 531
Kulkarni, V. P., Som, D., Morrison, S., et al. 2015, ApJ, 815, 24
Kumari, N., James, B. L., & Irwin, M. J. 2017, MNRAS, 470, 4618
Kumari, N., James, B. L., Irwin, M. J., Amorín, R., & Pérez-Montero, E. 2018, MNRAS, 476, 3793
Kunth, D., & Sargent, W. L. W. 1983, ApJ, 273, 81
Kunth, D., & Sargent, W. L. W. 1986, ApJ, 300, 496
Lagos, P., Demarco, R., Papaderos, P., et al. 2016, MNRAS, 456, 1549
Lagos, P., Scott, T. C., Nigoche-Netro, A., et al. 2018, MNRAS, 477, 392
Lagos, P., Telles, E., Nigoche-Netro, A., & Carrasco, E. R. 2012, MNRAS, 427, 740
Lebouteiller, V., Heap, S., Hubeny, I., & Kunth, D. 2013, A&A, 553, A16
Lebouteiller, V., Kunth, D., & Lequeux, J. 2004, A&A, 415, 55
Lebouteiller, V., Kunth, D., Lequeux, J., et al. 2006, A&A, 459, 161

Lebouteiller, V., Kunth, D., Thuan, T. X., & Désert, J. M. 2009, A&A, 494, 915
Lecavelier des Etangs, A., Désert, J. M., Kunth, D., et al. 2003, A&A, 413, 131
Lee, J. C., Gil de Paz, A., Tremonti, C., et al. 2009, ApJ, 706, 599
Legrand, F., Tenorio Tagle, G., Silich, S., Kunth, D., & Cervino, M. 2001, ApJ, 560, 630
Lelli, F., Verheijen, M., & Fraternali, F. 2014, MNRAS, 445, 1694
Lodders, K. 2003, ApJ, 591, 1220
López-Sánchez, Á R., Esteban, C., García-Rojas, J., Peimbert, M., & Rodriguez, M. 2007, ApJ, 656, 168
López-Sánchez, A. R., Dopita, M. A., Kewley, L. J., et al. 2012, MNRAS, 426, 2630
Mac Low, M. M., & Ferrara, A. 1999, ApJ, 513, 142
Makarov, D., Prugniel, P., Terekhova, N., Courtois, H., & Vauglin, I. 2014, A&A, 570, A13
Marino, A., Plana, H., Rampazzo, R., et al. 2012, MNRAS, 428, 476
Marino, R. A., Rosales-Ortega, F. F., Sanchez, S. F., et al. 2013, A&A, 559, A114
Martin, D. C., Fanson, J., Schiminovich, D., et al. 2005, ApJL, 619, L1
Matteucci, F., & Chiappini, C. 2005, PASA, 22, 49
McConnachie, A. W. 2012, AJ, 144, 4
McKinney, J. H., Jaskot, A. E., Oey, M. S., et al. 2019, ApJ, 874, 52
McQuinn, K. B. W., Skillman, E. D., Dolphin, A., et al. 2015, ApJL, 815, L17
McQuinn, K. B. W., Skillman, E. D., Heilman, T. N., Mitchell, N. P., & Kelley, T. 2018, MNRAS, 477, 3164
McQuinn, K. B. W., van Zee, L., & Skillman, E. D. 2019, ApJ, 886, 74
Melbourne, J., Phillips, A., Salzer, J. J., Gronwall, C., & Sarajedini, V. L. 2004, AJ, 127, 686
Milvang-Jensen, B., & Jørgensen, I. 1999, BaltA, 8, 535
Mollá, M., Vilchez, J. M., Gavilan, M., & Diaz, A. I. 2006, MNRAS, 372, 1069
Momcheva, I. G., Lee, J. C., Ly, C., et al. 2013, AJ, 145, 47
Morton, D. C. 2003, ApJS, 149, 205
Muratov, A. L., Kereš, D., Faucher-Giguère, C. A., et al. 2017, MNRAS, 468, 4170
Nava, A., Casebeer, D., Henry, R. B. C., & Jevremovic, D. 2006, ApJ, 645, 1076
Norberg, P., Cole, S., Baugh, C. M., et al. 2002, MNRAS, 336, 907
Orlitová, I., Verhamme, A., Henry, A., et al. 2018, A&A, 616, A60
Pearson, S., Besla, G., Putman, M. E., et al. 2016, MNRAS, 459, 1827
Pearson, S., Privon, G. C., Besla, G., et al. 2018, MNRAS, 480, 3069
Pérez-Montero, E., & Díaz, A. I. 2005, MNRAS, 361, 1063
Pettini, M., & Pagel, B. E. J. 2004, MNRAS, 348, L59
Ribaudo, J., Lehner, N., Christopher Howk, J., et al. 2011, ApJ, 743, 207
Richards, S. N., Schaefer, A. L., López-Sánchez, A. R., et al. 2014, MNRAS, 445, 1104
Ruffle, D. P., Hartquist, T. W., Caselli, P., & Williams, D. A. 1999, MNRAS, 306, 691
Salem, M., Besla, G., Bryan, G., et al. 2015, ApJ, 815, 77
Sánchez Almeida, J., Caon, N., Muñoz-Tuñón, C., Filho, M., & Cerviño, M. 2018, MNRAS, 476, 4765
Sánchez Almeida, J., Elmegreen, B. G., Muñoz-Tuñón, C., et al. 2015, ApJL, 810, L15
Sánchez Almeida, J., Elmegreen, B. G., Muñoz-Tuñón, C., & Elmegreen, D. M. 2014a, A&ARv, 22, 71
Sánchez Almeida, J., Morales-Luis, A. B., Muñoz-Tuñón, C., et al. 2014b, ApJ, 783, 45
Schlegel, D. J., Finkbeiner, D. P., & Davis, M. 1998, ApJ, 500, 525
Schneider, S. E., Thuan, T. X., Magri, C., & Wadiak, J. E. 1990, ApJS, 72, 245
Schulte-Ladbeck, R. E., Konig, B., Miller, C. J., et al. 2005, ApJL, 625, L79
Searle, L., & Sargent, W. L. W. 1972, ApJ, 173, 25
Sembach, K. R., & Savage, B. D. 1992, ApJS, 83, 147
Skillman, E. D., Côté, S., & Miller, B. W. 2003, AJ, 125, 610
Skillman, E. D., Salzer, J. J., Berg, D. A., et al. 2013, AJ, 146, 3
Stasinska, G. 2006, A&A, 454, L127
Stierwalt, S., Besla, G., Patton, D., et al. 2015, ApJ, 805, 2
Storchi-Bergmann, T., Calzetti, D., & Kinney, A. L. 1994, ApJ, 429, 572
Thuan, T. X., Etangs, A. L. d., & Izotov, Y. I. 2002, ApJ, 565, 941
Thuan, T. X., Izotov, Y. I., & Foltz, C. B. 1999, ApJ, 525, 105
Thuan, T. X., Lecavelier des Etangs, A., & Izotov, Y. I. 2005, ApJ, 621, 269
Tully, R. B. 1988, Nearby Galaxies Catalog (Cambridge: Cambridge Univ. Press)
Tully, R. B., Courtois, H. M., & Sorce, J. G. 2016, AJ, 152, 50
van Zee, L., & Haynes, M. P. 2006, ApJ, 636, 214
Vilchez, J. M., & Iglesias Páramo, J. 1998, ApJ, 508, 248
Vilchez, J. M., Pagel, B. E. J., Díaz, A. I., Terlevich, E., & Edmunds, M. G. 1988, MNRAS, 235, 633
Williamson, D., & Martel, H. 2018, ApJ, 867, 72
Williamson, D., Martel, H., & Romeo, A. B. 2016, ApJ, 831, 1
Wright, A. C., Brooks, A. M., Weisz, D. R., & Christensen, C. R. 2019, MNRAS, 482, 1176
Wright, E. L., Eisenhardt, P. R. M., Mainzer, A. K., et al. 2010, AJ, 140, 1868